BRL

AD

MEMORANDUM REPORT NO. 2796

(Supersedes IMR No. 233)

MISSILE WARHEAD MODELING: COMPUTATIONS AND EXPERIMENTS

William W. Predebon
Walter G. Smothers
Charles E. Anderson

October 1977

USA ARMAMENT RESEARCH AND DEVELOPMENT COMMAND
USA BALLISTIC RESEARCH LABORATORY
ABERDEEN PROVING GROUND, MARYLAND

DISCLAIMER NOTICE

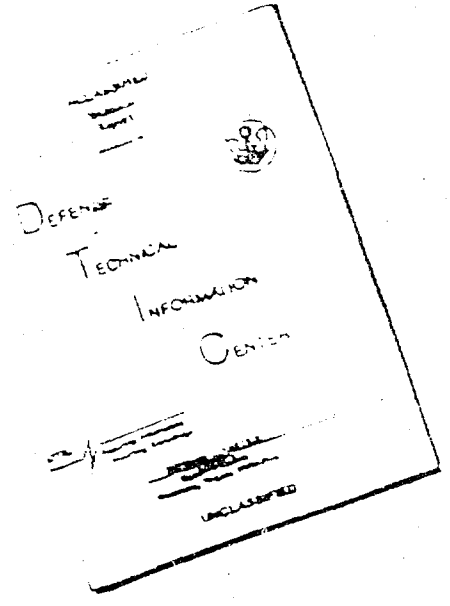

THIS DOCUMENT IS BEST QUALITY AVAILABLE. THE COPY FURNISHED TO DTIC CONTAINED A SIGNIFICANT NUMBER OF PAGES WHICH DO NOT REPRODUCE LEGIBLY.

Destroy this report when it is no longer needed.
Do not return it to the originator.

Secondary distribution of this report by originating or sponsoring activity is prohibited.

Additional copies of this report may be obtained from the National Technical Information Service, U.S. Department of Commerce, Springfield, Virginia 22161.

The findings in this report are not to be construed as an official Department of the Army position, unless so designated by other authorized documents.

The use of trade names or manufacturers' names in this report does not constitute indorsement of any commercial product.

UNCLASSIFIED (14) BRL-MR-2796

SECURITY CLASSIFICATION OF THIS PAGE (When Data Entered)

REPORT DOCUMENTATION PAGE

READ INSTRUCTIONS BEFORE COMPLETING FORM

1. REPORT NUMBER: BRL Memorandum Report No. 2796
2. GOVT ACCESSION NO.
3. RECIPIENT'S CATALOG NUMBER

4. TITLE (and Subtitle): (6) MISSILE WARHEAD MODELING COMPUTATIONS AND EXPERIMENTS.
5. TYPE OF REPORT & PERIOD COVERED: (9) Final rept.
6. PERFORMING ORG. REPORT NUMBER

7. AUTHOR(s): (10) William W. Predebon, Walter G. Smothers, Charles E. Anderson
8. CONTRACT OR GRANT NUMBER(s)

9. PERFORMING ORGANIZATION NAME AND ADDRESS: USA Ballistic Research Laboratories, Aberdeen Proving Ground, MD 21005
10. PROGRAM ELEMENT, PROJECT, TASK AREA & WORK UNIT NUMBERS: (16) 1L161102AH43

11. CONTROLLING OFFICE NAME AND ADDRESS: US Army Materiel Development & Readiness Command, 5001 Eisenhower Avenue, Alexandria, VA 22333
12. REPORT DATE: (11) OCT [redacted] 77
13. NUMBER OF PAGES: 56 (12) 52p.

14. MONITORING AGENCY NAME & ADDRESS (if different from Controlling Office)
15. SECURITY CLASS. (of this report): UNCLASSIFIED
15a. DECLASSIFICATION/DOWNGRADING SCHEDULE

16. DISTRIBUTION STATEMENT (of this Report)

Approved for public release; distribution unlimited.

17. DISTRIBUTION STATEMENT (of the abstract entered in Block 20, if different from Report)

18. SUPPLEMENTARY NOTES

Supersedes Interim Memorandum Report No. 233 dated June 1974.

19. KEY WORDS (Continue on reverse side if necessary and identify by block number)

Hemp computations
Velocity vector predictions
SAM-D
Anti-aircraft warheads
Preformed fragments
Warhead Modeling
Explosive testing
Liner effects
Geometrical variations
Fragment recovery testing
Radiographic techniques

20. ABSTRACT (Continue on reverse side if necessary and identify by block number) (klb)

A computational warhead modeling capability has been developed which models the effects of warhead length to diameter ratio, and confinement variation, explosive material and initiation posture, and internal cavity shape and material. These effects are modeled with a time-dependent, two-dimensional, Lagrangian finite - difference computer code, integrally modified to include fragment separation (or fragmentation for continuous warheads) and subsoquent explosive gas leakage between fragments.

DD FORM 1 JAN 73 1473 EDITION OF 1 NOV 65 IS OBSOLETE

050750

UNCLASSIFIED
SECURITY CLASSIFICATION OF THIS PAGE (When Data Entered)

20. (Cont.) Experimental results of a variety of modeled missile warheads (discrete-fragment warheads) are presented and compared with the computational results. In the experiments the fragment speed and angle distributions with respect to their original position on the warhead are determined through time-sequential, orthogonal flash radiography of the warhead fragment spray in flight, and soft recovery of the fragments after launch.

TABLE OF CONTENTS

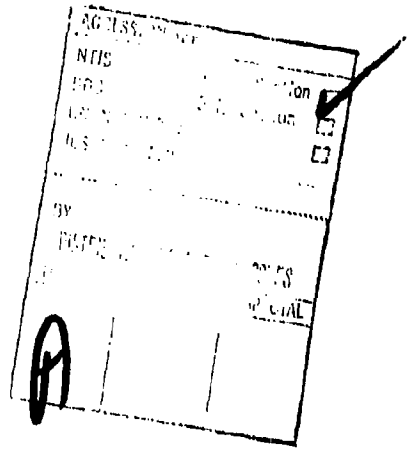

LIST OF ILLUSTRATIONS

LIST OF ILLUSTRATIONS (Cont.)

LIST OF ILLUSTRATIONS (Cont.)

I. INTRODUCTION

Missile warheads are generally quite different in design and construction than warheads used in other military applications, such as artillery shells. This difference mainly is a consequence of the low launch loads experienced by missile warheads. Warhead design in applications where high launch loads are experienced (artillery shells) are usually of the natural fragmentation or controlled fragmentation type. By way of background, natural fragmentation warheads are continuous metal casing warheads with no preselected control sites of failure. Controlled fragmentation warheads, on the other hand, are continuous warheads with preselected control sites or lines of failure. These failure sites are usually arrived at mechanically, metallurgically or explosively. However, missile warheads are generally discrete-fragment warheads and not continuous metal-casing systems. Discrete-fragment warheads are preformed-fragment warheads in which the fragments of the desired shape and mass are placed on a liner (metal or plastic) which encases the high explosive. The warhead is then placed inside a missile casing (skin). These preformed-fragments are attached to the liner and neighboring fragments by an epoxy filler. Due to the very low launch load environment of a missile, this evidently is sufficient for structural integrity.

In the past the main analytical method for predicting fragmentation warhead performance*, i.e., fragment speed and direction, has been the Gurney[1] and Taylor[2] formulae. These formulae are one-dimensional by assumption and the Gurney formula requires an empirically determined constant. This constant, called the Gurney constant, is obtained experimentally via warhead tests for each different situation. Due to the one-dimensional nature of these formulae, their utility for predicting warhead performance near the ends is questionable. It has been shown[3] that for cases when the flow is essentially one-dimensional, such

Warhead performance as used in this report will mean fragment velocity distribution, which, it can be shown, yields fragment mass distribution.

[1] *Gurney, R. W., "The Initial Velocities of Fragments from Bombs, Shells and Grenades", BRL Report 405, September 1943, AD#36218.*

[2] *Birkhoff, G., MacDougall, P., Pugh, E. M. and Taylor, G. I., Sir., "Explosives with Lined Cavities", J. Appl. Phys., Vol. 19, p. 563, June 1948.*

[3] *Karpp, R. R. and Predebon, W. W., "Calculations of Fragment Velocities from Naturally Fragmenting Munitions", BRL Memorandum Report No. 2509, July 1975.* (AD #B007377L)

as long artillery projectiles (L/D > 2), these formulae are adequate for predicting fragment velocity. However, for cases where the flow is two-dimensional, such as near the warhead ends for any size projectile, and for axisymmetric warheads with length to diameter ratios less than or equal to two, these formulae are inadequate[3]. Lastly, these formulae were initially derived for continuous warheads (i.e., natural fragmentation warheads) and for one specific initiation posture. Consequently, for discrete-fragment warheads, these formulae are not applicable without significant modification and experimental recalibration.

In an effort to find a method to predict warhead performance not only over its midsection but over its entire length including the ends, a time-dependent, two-dimensional, Lagrangian computer code has been applied to naturally fragmenting warheads. In Reference 3, finite-difference calculations of warheads with varying explosive fills and casing materials were compared with experimental results; good agreement was demonstrated. However, the computer code used to obtain the calculations in Reference 3 assumes a continuum. Warheads eventually fragment, and after fragmentation the continuum assumption needs to be modified. A method to model the effects of fragmentation and subsequent explosive gas leakage was presented in Reference 3 as an integral part of the computational scheme.

In this report the earlier work by Karpp and Predebon[3] on natural fragmenting warhead is extended to missile warheads, i.e., discrete-fragment warheads. The objective of the work reported here was to develop a warhead modeling capability to predict the performance of missile warheads in general, as well as warhead designs pertinent to the "Focused-Blast-Fragment" advanced development program.* Computational modeling was emphasized with limited experimental verification as needed.

In the next section the experimental program is discussed in detail. In Section III the computational modeling is explained. Comparisons between the computational and experimental results are discussed in Section IV. The conclusions and recommendations follow in Section V.

*This work was supported by the BRL, Picatinny Arsenal and AMC, HQ.

II. EXPERIMENTAL PROGRAM

Figure 1 is a schematic drawing of part of a typical test set-up used in the warhead test firings for this program. Shown is the warhead on an angled* wood stand which rests on metal plates on the floor of the second level of the test facility. The two metal plates form a preset aperture through which passes the column of fragments to be radiographed. The lower level of the test facility contains two orthogonal banks (each bank has four flash x-ray tubes) which provide time-sequential, orthogonal radiography.

Due to the funding and time constraints on part of this program, it became obvious at the very beginning that cubical fragments** could not be placed completely around each test warhead and still complete the minimum number of warhead tests planned. Also, from a long term point of view, it is desirable to have a more economical method for testing preformed-fragment warheads. The method used determined the minimum azimuthal-sector angle containing preformed-fragments which adequately represented the situation where the entire cylindrical warhead contained preformed-fragments. All the warheads tested had an overall cylindrical shape. Figure 2 illustrates a test warhead with an azimuthal fragment-bearing sector angle of 22.5° for a typical length to diameter (L/D) ratio of 2.0. In all tests where an azimuthal sector of the warhead contained the preformed-fragments, the remainder of the warhead contained strips (rods) of the same material. The width of the strips was equal to the width of the fragments (for proper radial explosive gas leakage), and the strip lengths were equal to the explosive charge length.

Table I contains all the characteristics of the test warheads by their respective round number. As indicated in Table I, the warhead length to diameter ratio was varied from 1.0 to 2.0. The explosive charge in all cases was Octol (25% TNT, 75% HMX). The fragments were steel (AISI 1018 or 1020) cubes and, in all but one test, were placed directly on the bare explosive charge. This type of configuration was adopted in order to determine with greater accuracy the effect which explosive gas leakage between fragments has on the fragment velocity distribution, particularly for the computational modeling portion of the program.

Figures 3 and 4 illustrate typical radiographic results from L/D = 1.0 and L/D = 2.0 warheads, respectively. Both test warheads were initiated on the axis at the left end. Figures 3 and 4 show the longitudinal and orthogonal views of the fragment distributions in their actual spacial positions at two different times. In each of the test cases the fragments in the radiographed column were premarked for identification and were recovered in Celotex. The spacial location of the recovered premarked

The angled wood stand is used to rotate the main fragment distribution into the available radiographic view.

**In all the warhead tests the fragment shape was cubical.*

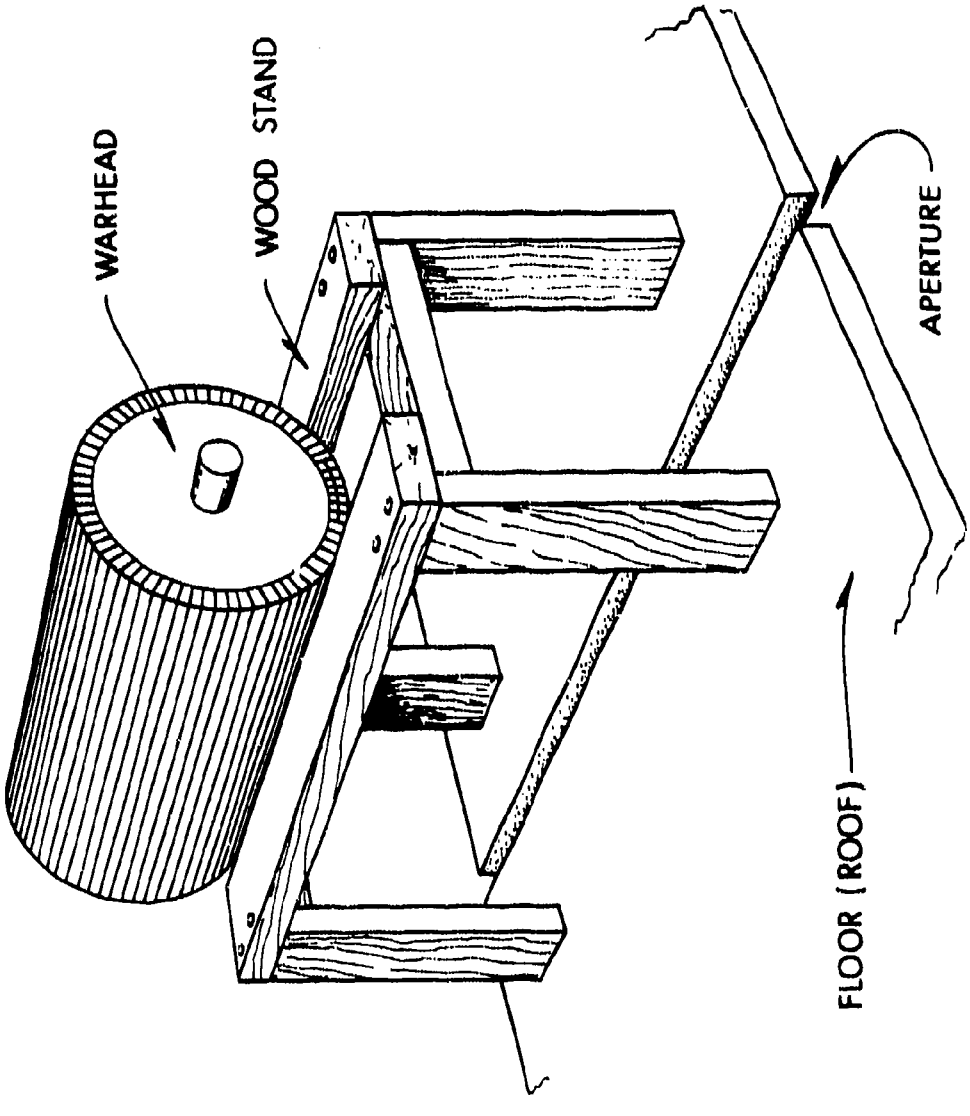

Figure 1. Typical Test Configuration

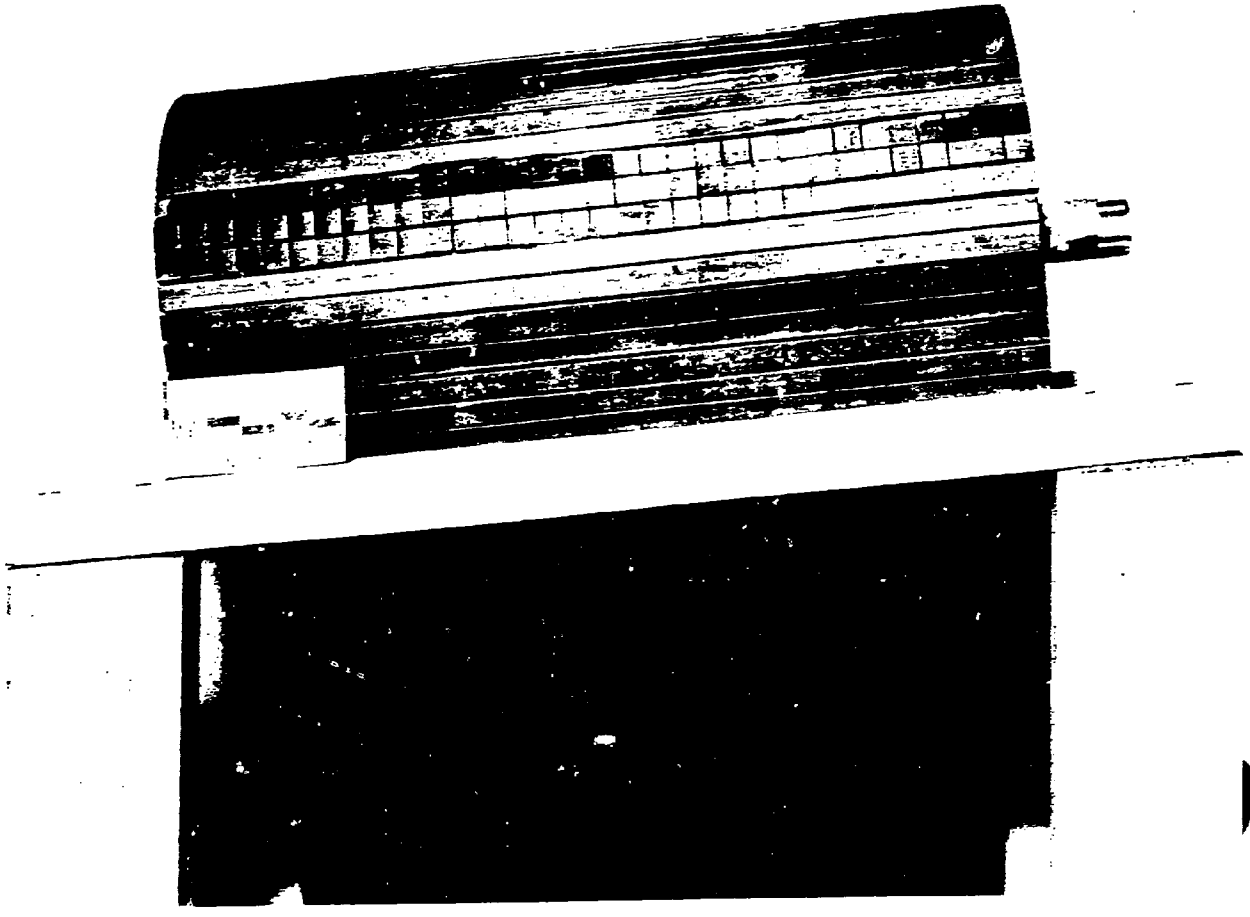

Figure 2. Test Warhead of L/D = 2.0, with Azimuthal Fragment-Bearing Sector Angle of 22.5°

TABLE I. WARHEAD CHARACTERISTICS AND TEST DATA

Round No.	$\frac{L_{HE}}{D_{HE}}$	D_{HE}	Fragment Layers	α_f	N_{cc}	N_c	N_R	L_c[1]	M_c[1]	M_R[1]	M_{HE}	M_T	$\bar{C}/H$	M_{RC}[1]	h_{RC}[1,2]	$\frac{R_h}{R_o}$	D_m	Initiation[4]
		mm		Degrees				mm	GM	GM	GM	GM		GM	mm		mm	
9237	1	126.04	1	22.5	16	3	47	7.89	3.84	--	2875	5082	.933	3.64	9.58	1.21	140.09	SEA
9310	1	126.04	1	45	16	7	43	7.92	3.87	60.8	2881	5073	.938	3.77	9.37	1.18	140.95	SEA
9264	1	126.04	1	90	16	13	37	7.89	3.84	61.4	2880	5042	.947	3.65	9.75	1.24	140.81	SEA
9242	2	126.04	1	22.5	32	3	47	7.89	3.84	122.7	5743	6136	.936	3.69	9.49	1.20	140.92	SEA
9285	2	126.04	1	45	32	7	43	7.87	3.81	122.0	5743	6099	.942	3.67	9.53	1.21	140.84	SEA
9302	2	126.04	1	45	32	7	43	7.92	3.87	123.0	5729	6155	.931	3.72	9.95	1.26	140.97	SEA
9363	2	126.04	1	90	32	13	36.5	7.95	3.91	124.8	5740	6199	.926	3.80	9.72	1.22	141.07	SEA
9415	2	126.04	1	135	32	19	30.5	7.95	3.92	124.8	5740	6201	.926	3.78	9.79	1.23	141.07	SEA
9323	2	126.04	1	45	32	7	42	7.93	3.89	123.9	5744	6077	.945	3.70	9.55	1.20	140.79	DEA
9317	2	126.04	2[5]	45	63	13	85	3.96	0.486	62.3	5745	6081	.945	0.458	4.67	1.18	140.80	SEA
9342	2	126.04	2[6]	45	63	13	84.25	3.96	0.485	63.7	5732	6039	.949	0.464	4.75	1.21	140.70	SEA
9457[7]	2	125.98	1	90	31	13	37	7.96	3.93	127.8	5608	6313	.889	3.80	9.97	1.25	144.11	SEA

[1] These data represent the average value of the variable.

[2] M_{RC} represents the measured cube dimension in the hoop direction for the recovered cubes.

[3] R_h/R_o is the expansion ratio at fragment separation which is equivalent to M_{RC}/L_C.

[4] SEA refers to single end axial initiation and DEA refers to dual end axial initiation.

[5] The fragment layers in this test were aligned (See Section II).

[6] The fragment layers in this test were bricked (See Section II).

[7] The liner was 6061-T4 aluminum with a nominal wall thickness of 1.60 mm and total mass of 441 GM. The endplates were 2024-T3 aluminum with a nominal thickness of 6.35 mm and with total masses of 275 GM (detonator endplate) and 279 GM for the other end plate.

Figure 3. Typical Radiographic Results for L/D = 1.0 Warhead

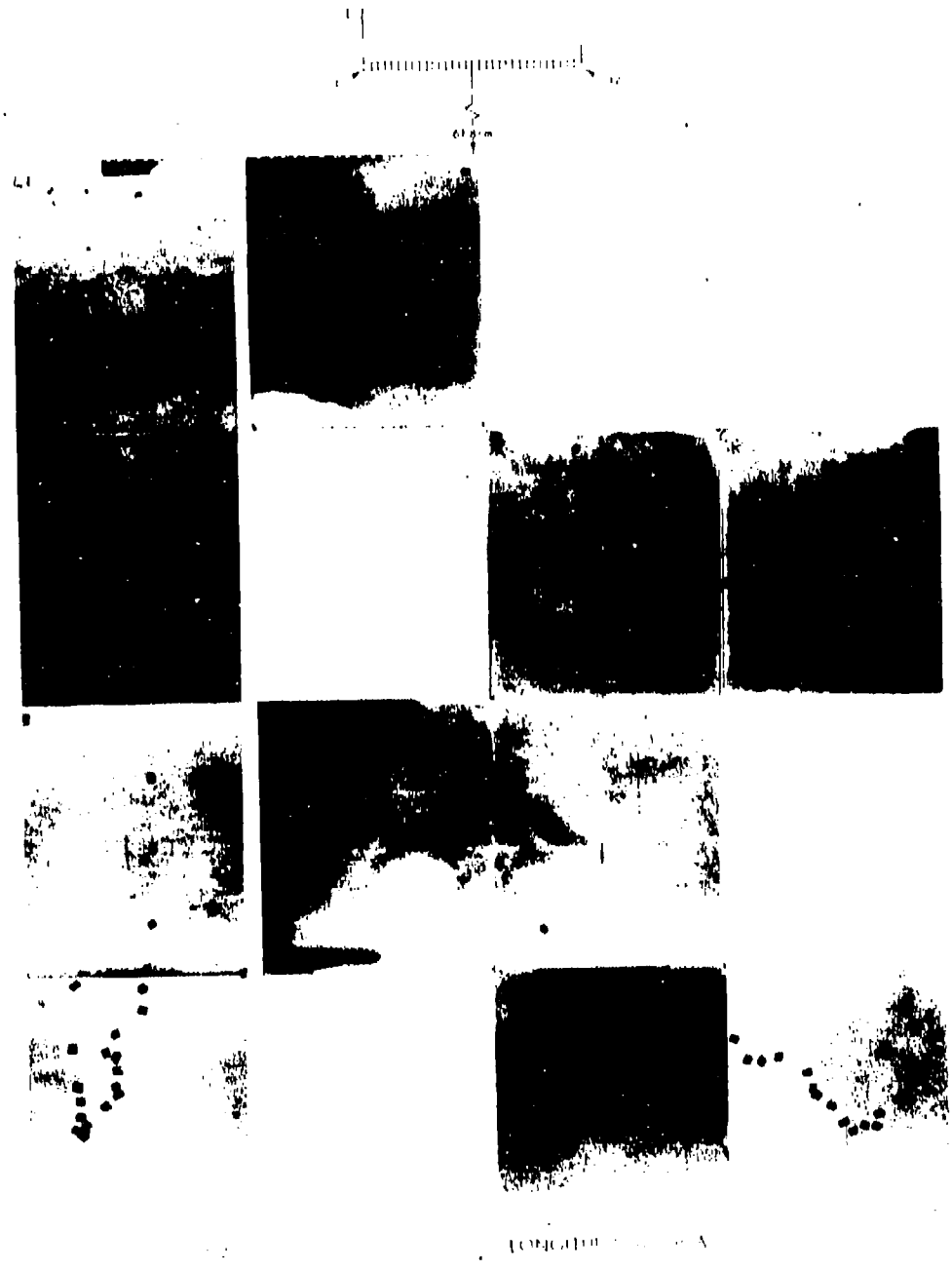

Figure 4. Typical Radiographic Results for L/D = 2.0 Warhead

fragments, in conjunction with the time-sequential, orthogonal radiography of the fragments, permitted development of the results shown in Figures 5 and 6 for the two tests illustrated in Figures 3 and 4. In Figures 5 and 6, each of the fragments in flight are labeled according to their original position on the warhead (shown at the top of the figures). Two different times are shown for both longitudinal and orthogonal views.

To illustrate radiographically the fragment focusing that can be achieved, Figure 7 shows (for two different times) the longitudinal and orthogonal views of an L/D = 2.0 warhead which was initiated simultaneously at both ends on the axis of symmetry. The fragments of Figure 7 are labeled in Figure 8 according to their original position on the warhead. Again two different times are shown for the longitudinal and orthogonal views.

To determine the accuracy of the experimental procedure, a simple error analysis of the measurements was conducted and the round to round variation was quantified. Using a conservative approach to error analysis wherein only maximum differences are considered, for two time-sequential observations of fragments the measurement uncertainty in the fragment speed is less than ± 1% and is less than ± 0.004 for the tangent of the fragment projection angle. The round to round variation in the warhead tests is shown in Figure 9. Plotted in Figure 9 is the fragment speed and projection angle distributions versus fragment number or relative initial axial position from two tests of nominally identical (See Table I) L/D = 2.0 cylindrical warheads. The round to round variation in fragment speed is ± 3% for two time-sequential observations of the fragments and ± 13% for single time observations of fragments (which occurs for a few fragments at both ends). The overall round to round variation in the tangent of the fragment projection angle is ± 0.02. Therefore, it appears that the variations from one round to another (nominally the same) are larger than the measurement uncertainty. Consequently, it was inadvisable to attempt to improve the accuracy of the measurement procedure.

As previously mentioned, the cubical fragments were placed on the warhead in varying azimuthal sector angles, with strips in the remaining azimuthal angle, to determine the minimum azimuthal fragment-bearing sector angle required to approximate the situation in which fragments covered the entire round. Plotted in Figures 10 and 11 are the fragment speed and projection angle distributions for varying azimuthal fragment-bearing sector angles α for L/D = 1.0 and 2.0 warheads, respectively. Since the percent difference between the $\alpha = 45°$ and $\alpha = 90°$ cases in Figure 10 is within round to round variation shown in Figure 9, it is felt that a 45° azimuthal fragment-bearing sector angle is adequate for the L/D = 1.0 case. For the L/D = 2.0 case, Figure 11 indicates a large difference between $\alpha = 22.5°$ and $\alpha = 45°$, 90° and 135°. However the differences are much smaller between the $\alpha = 45°$, 90° and 135° cases, although the fragment speeds for $\alpha = 45°$ tend to be greater than or

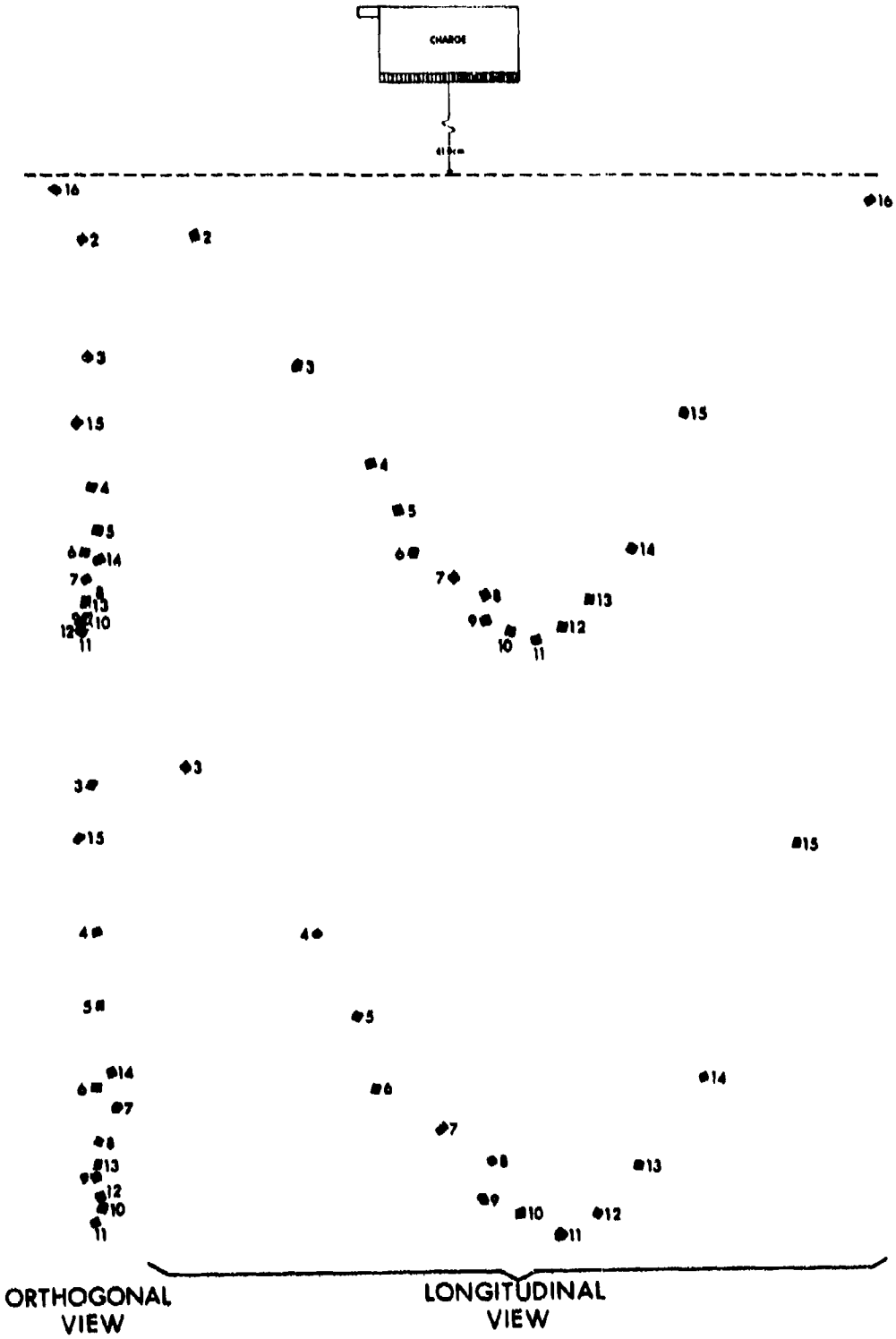

Figure 5. Identification of Fragments in Figure 3

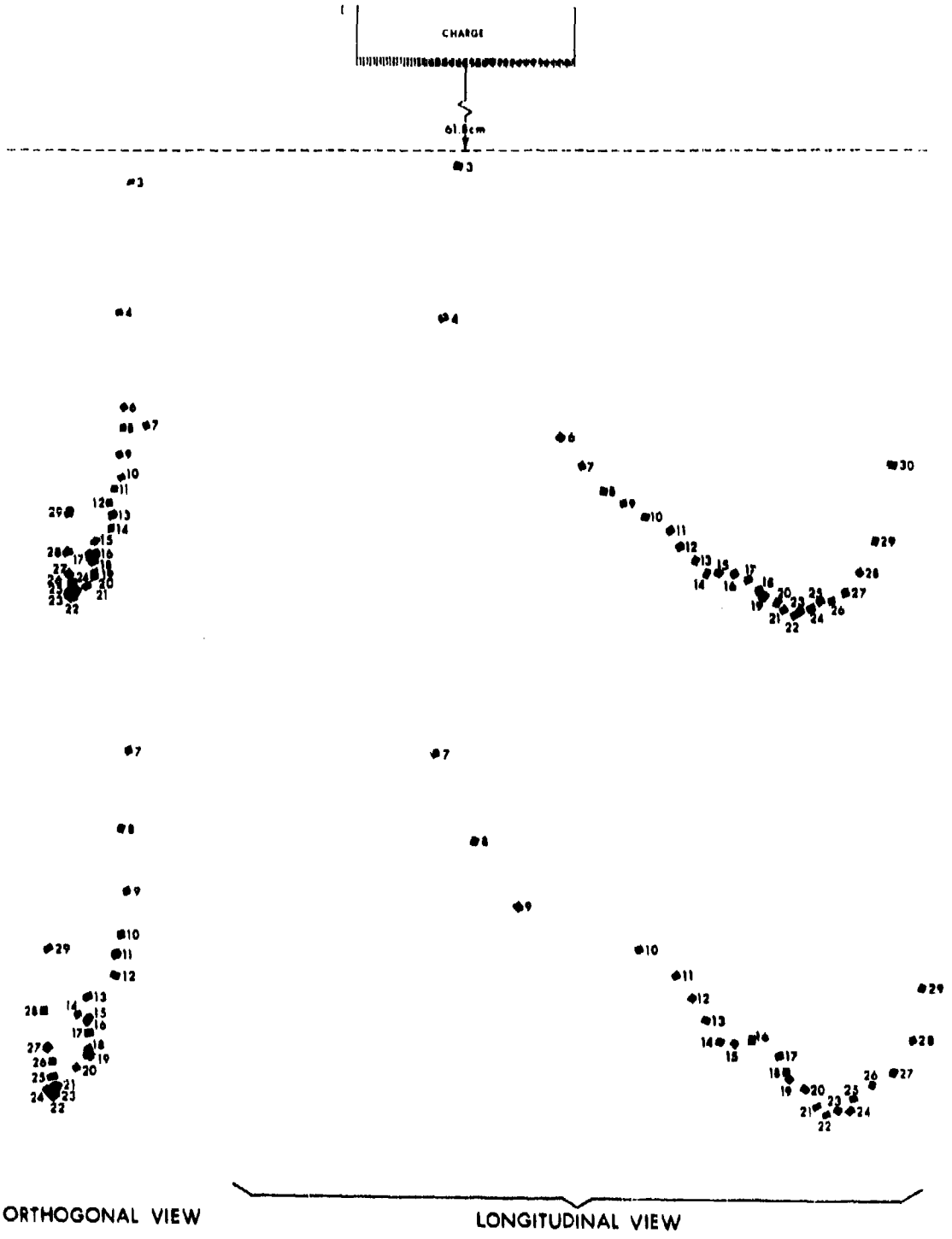

Figure 6. Identification of Fragments in Figure 4

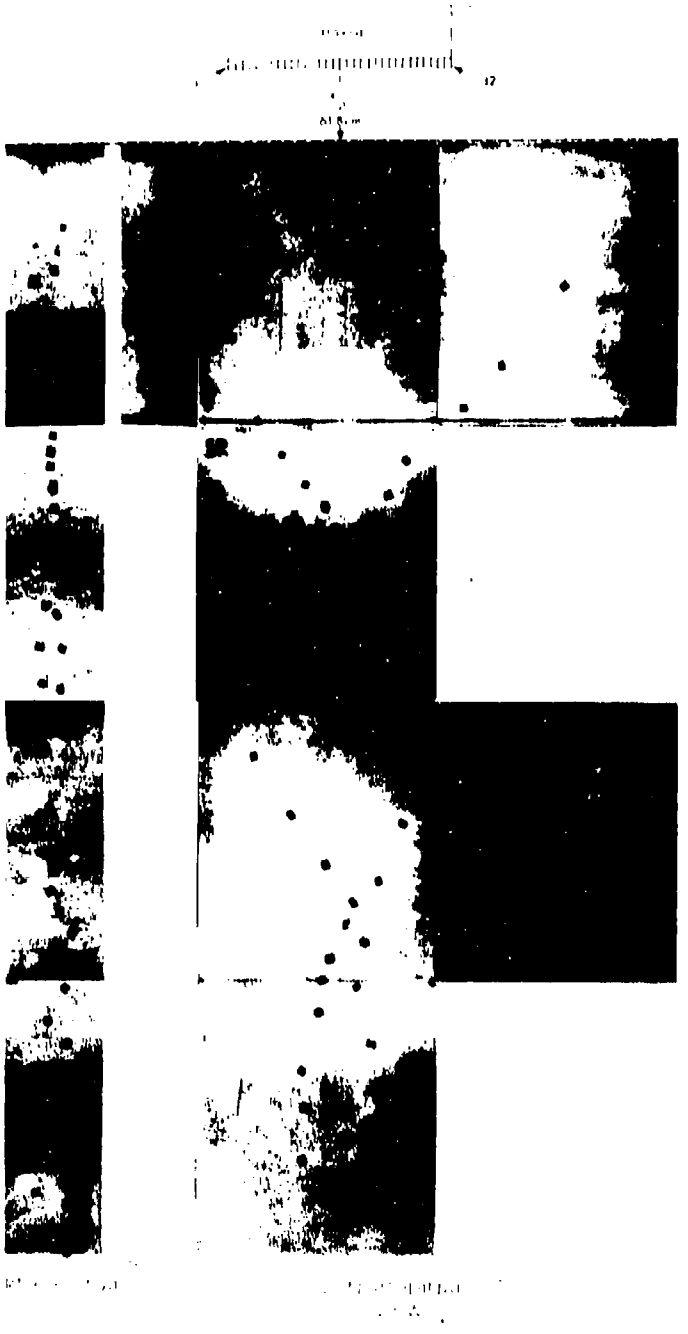

Figure 7. Radiographic View of Fragment Focusing, L/D = 2.0: Dual End Axial Initiation

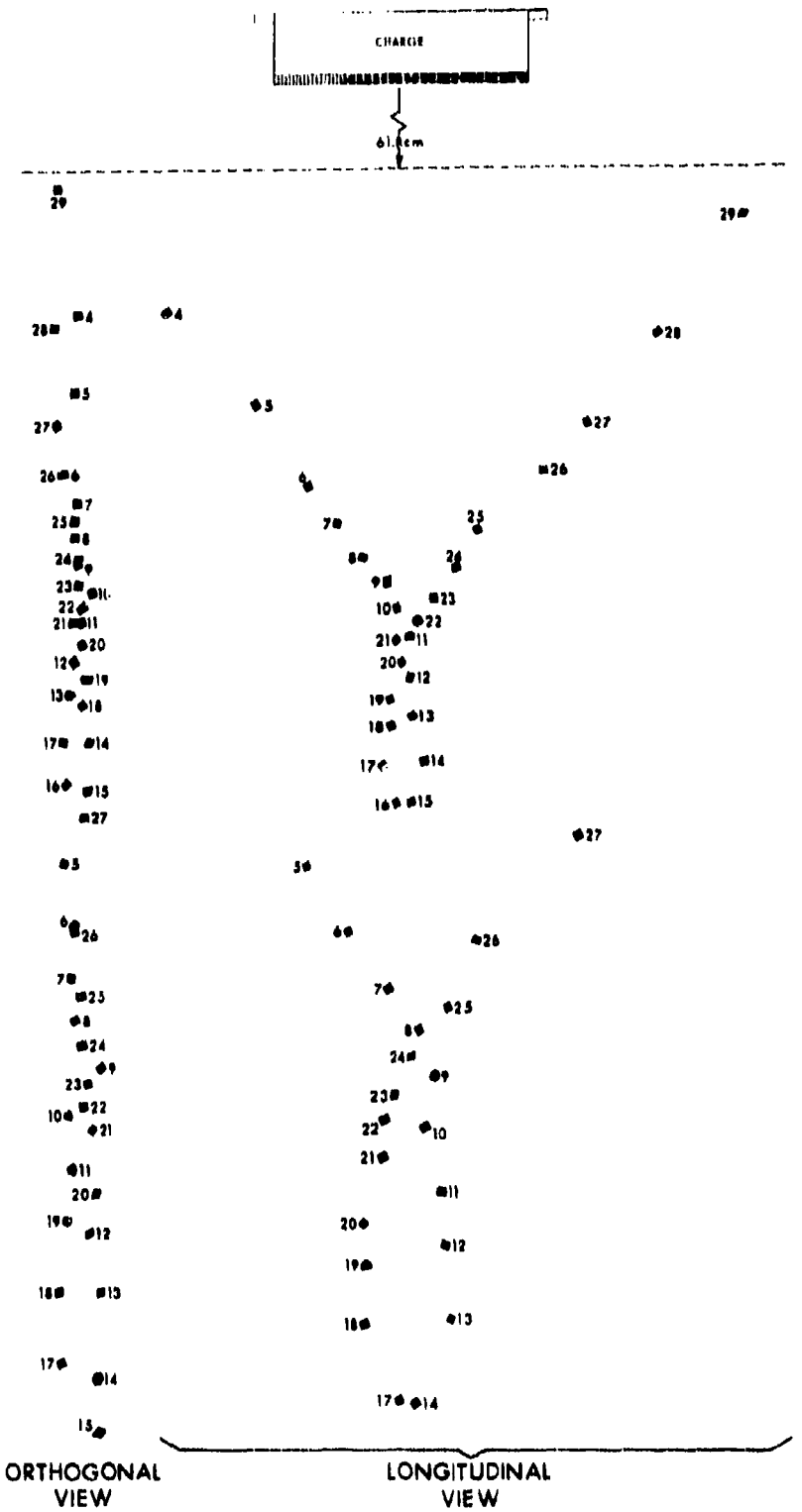

Figure 8. Identification of Fragments in Figure 7

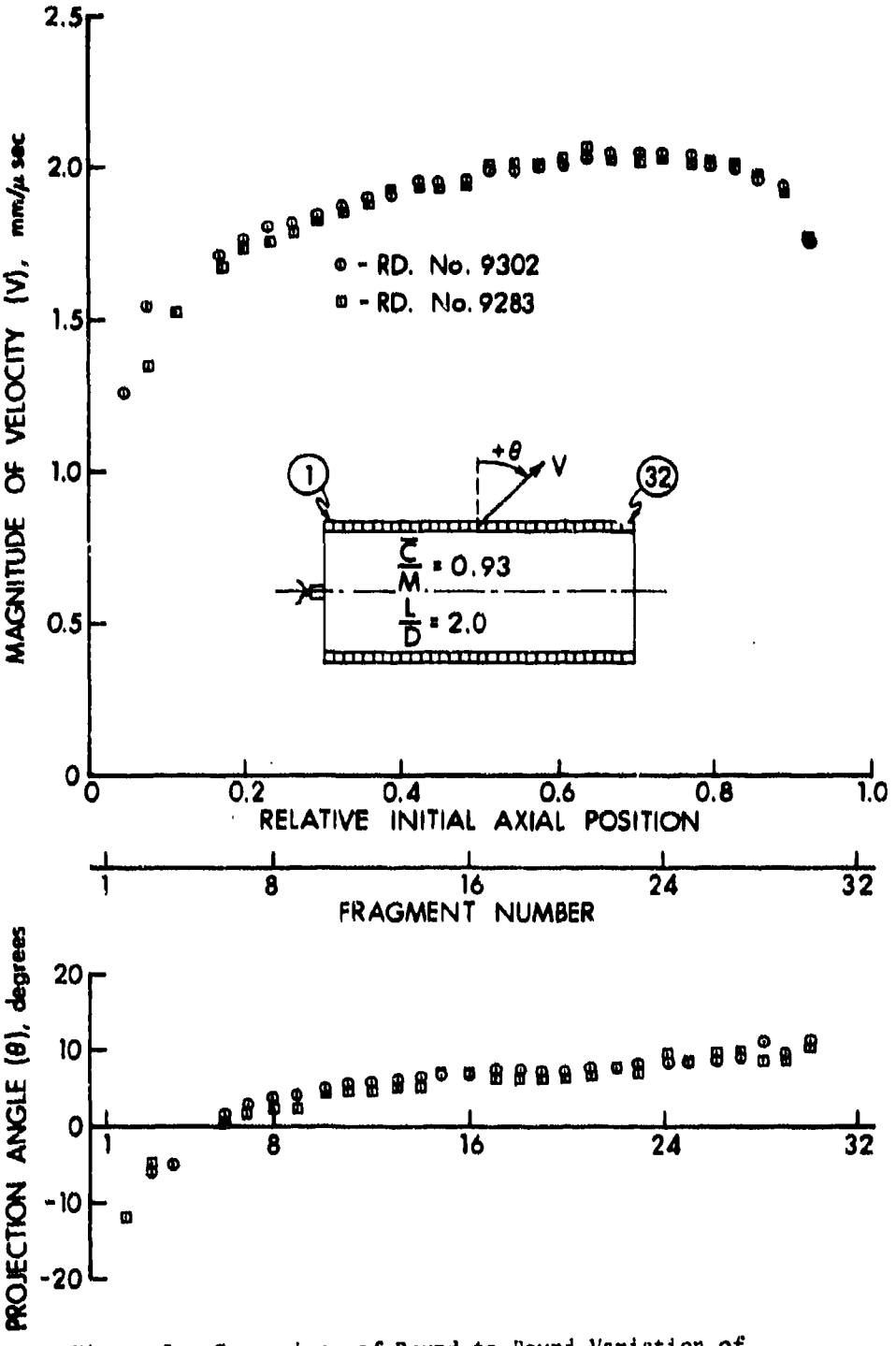

Figure 9. Comparison of Round to Round Variation of Warhead Tests

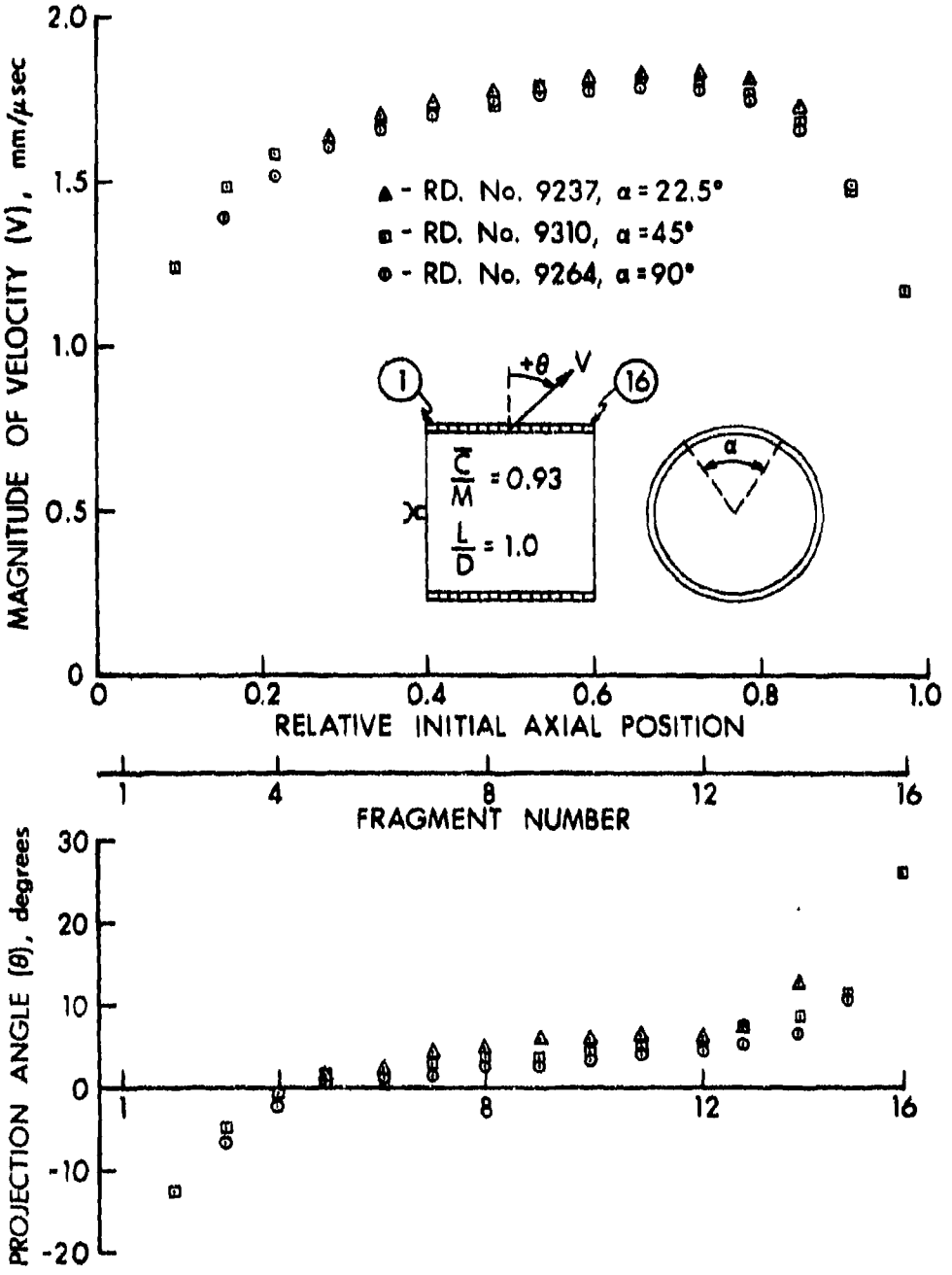

Figure 10. Variation of "Warhead Performance" with Azimuthal Fragment-Bearing Section Angle, L/D = 1.0

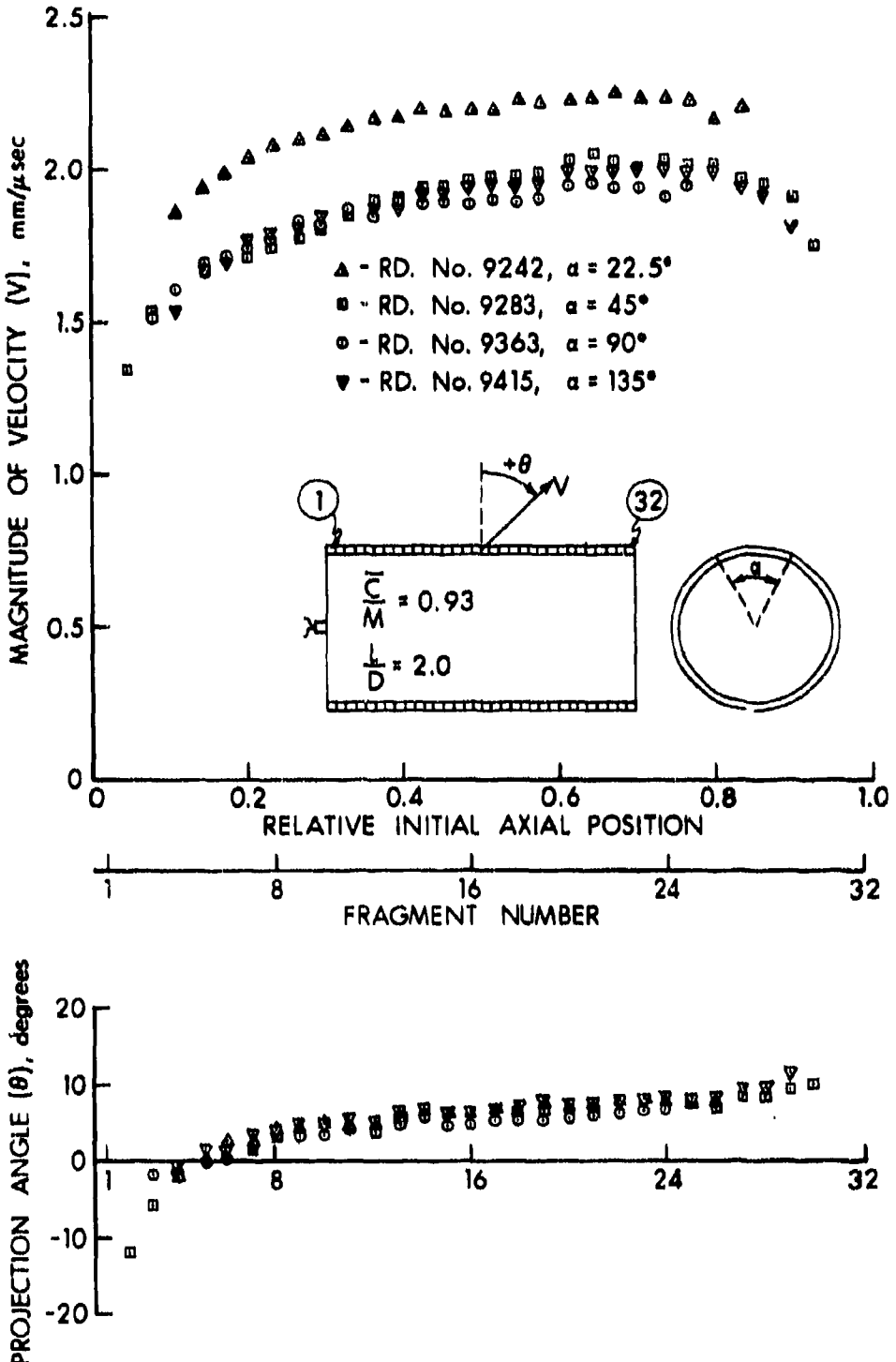

Figure 11. Variation of "Warhead Performance" with Azimuthal Fragment-Bearing Section Angle, L/D = 2.0

equal to $\alpha = 90°$ or $\alpha = 135°$, especially in areas remote from end rarefactions. Mindful of the latter point and the round to round variation shown in Figure 9, the variation in fragment speed between the $\alpha = 90°$ and 135° is within the round to round variation; whereas the same variation between the $\alpha = 45°$ and 90° is generally not. In view of the above it is felt that $\alpha = 90°$ is desirable for the L/D = 2.0 case.

Returning to the $\alpha = 22.5°$ case in Figure 11, due to the unexpected large differences between it and $\alpha = 45°$, 90° and 135°, particularly near the ends where one would expect the fragment speeds to converge to a common value for most practical α's, it is questionable whether these large differences are due to increased confinement for $\alpha = 22.5°$ or perhaps some uncovered error in the data. An additional test at $\alpha = 22.5°$ will be required to clarify these questions; however, it was judged that the results of such a test would not significantly change the main thrust and purpose of this study and therefore was not completed at this time.

The experimental results of cases in which computational results were obtained are discussed in Section IV. There are a few test cases for which the computations were not performed during this program and these experimental results will be presented at this time.

The modeling of multi-fragment layering is immensely complicated due to the many combinations of layer patterns that can be placed on the warhead. In order to bracket the effects of the simplest multi-fragment layering case, i.e., two layers of fragments, two double-layered discrete-fragment warheads were fired. The fragment layers were aligned with respect to each other for the first warhead; the other warhead had the fragments bricked (that is, the fragments on the top layer were displaced by a distance equal to half of a cube side relative to the fragments on the bottom layer). In Figure 12 are plotted the results of the aligned and bricked double-layered warheads. In order to compare these results to the single layered test, the charge mass to metal mass (C/M), the type of explosive, explosive initiation and explosive dimensions were kept the same as the single layered L/D = 2.0 case (shown in Figure 16). Further, the fragment shape and fragment material were kept the same. These constraints thus imposed that the double-layered fragment masses be 1/8 the single layered masses. Due to the resulting lower cube masses (0.486 gm), and therefore much smaller dimensions, the previously used cube numbering system was not effective in identifying the cubes with respect to their original position on the warhead. When the cubes were recovered they had generally collided with each other during flight and the punched numbers on each fragment were unidentifiable. Consequently the fragment speed is plotted with respect to its projection angle in Figure 12 rather than its initial position on the warhead.

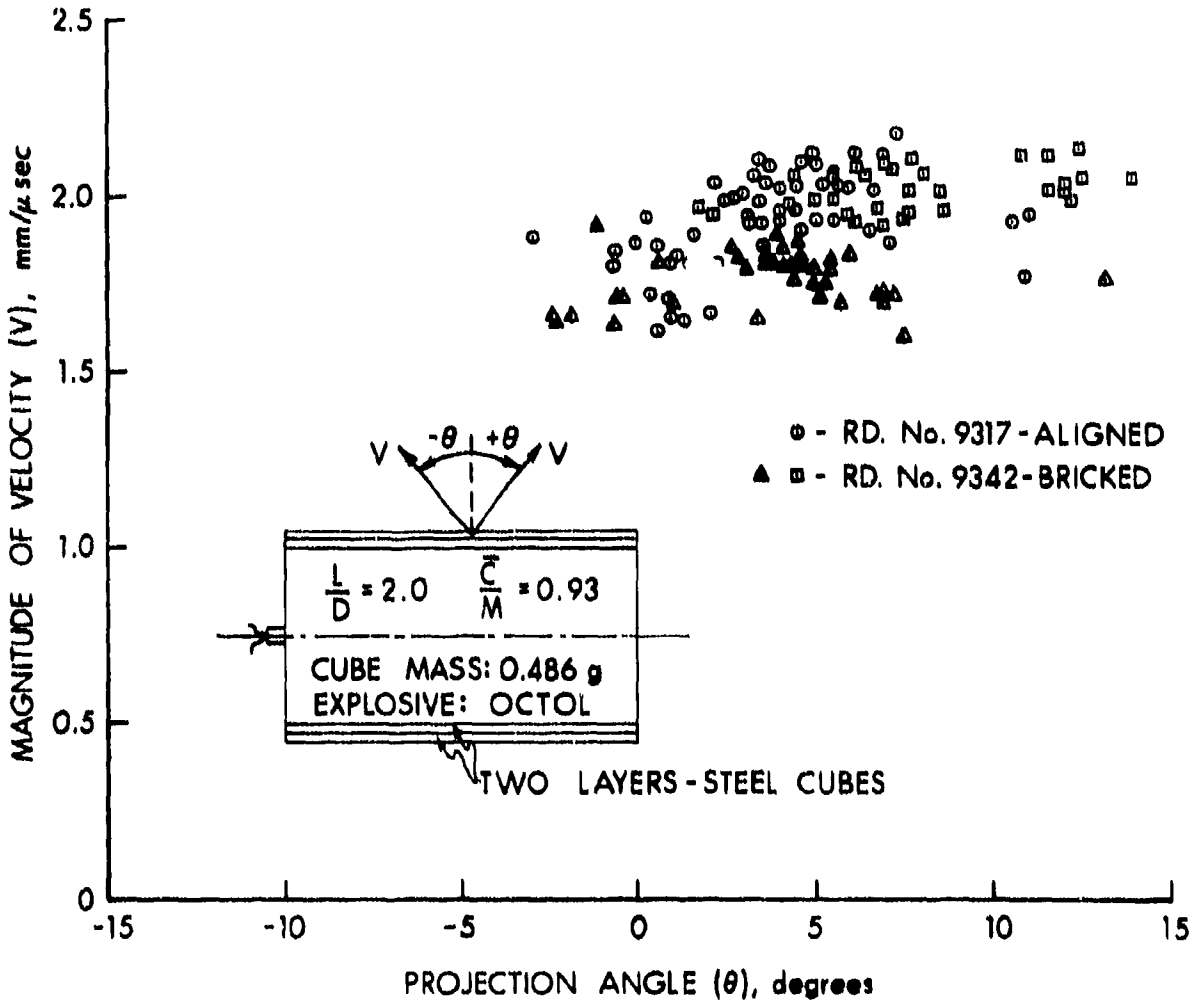

Figure 12. Double-Layered Discrete-Fragment Warheads: Fragment Speed Versus Projection Angle

In Figure 12 it is quite evident that there exists a significant variation of the magnitude of the velocity at any projection angle; this observation applies both to the aligned and bricked warheads. By comparison, if the data from the single fragment layer case of Figure 16 were plotted versus projection angle, as in Figure 12, only one fragment would appear at any particular projection angle. It is important to note, for reasons previously discussed, it was very difficult to identify the same fragment in two time-sequential, radiographic views for many of the fragments in the double-layered cases. Consequently, the only fragments that are plotted are those in which this identification was confidently made. Therefore, although the single fragment layer case cannot be compared with the double-layered case over the entire projection angle distribution, meaningful comparisons can be made over the projection angle range for which data were obtained. In the two examples depicted in Figure 12, the spread in the speeds ranges from 0.15 to 0.40 mm/μsec over the projection angle distribution. The most probable contributing cause of this spread in speed at a given projection angle is slippage between the layer fragments. Thus, instead of fragments leaving the warhead at a given angle having one particular velocity, collective effects result in a number of fragments with varying velocities at the specified angle.

It is lastly noted that the plotted speeds in Figure 12 have not been corrected for drag, which from the data was estimated to be causing a 4%-7% decrease in fragment speeds. This decrease was obtained by comparing single and double flash calculations of identical cubes. This calculation was also completed in the single layered cases; however, in these cases the drag was always negligible. Because of the lower cube masses (0.486 gm) in the double-layered warheads, drag is no longer negligible.

Shown in Figure 13 are the experimental results for single-layered fragments on an aluminum liner with aluminum endplates, L/D = 2.0 cylindrical warhead. As shown, initiation was on the axis on the left side of the warhead. All the necessary data are given in Table I. This is the only test case reported with a liner and endplates. These results will be discussed in some detail in Section IV along with a similar test case without a liner and endplates.

III. COMPUTATIONAL MODELING

The computer code that is being used for the computation modeling is a modified version of the HEMP[4] computer code. The HEMP code, which was originally developed at the Lawrence Livermore Laboratories, California, is a time-dependent, two-dimensional, Lagrangian finite-difference code.

---

[4] *Wilkins, M. L., "Calculations of Elastic-Plastic Flow," Methods of Computational Physics, Vol. 3, edited by Alder, B., Fernback, S. and Rotenburg, M., Academic Press, NY, 1964.*

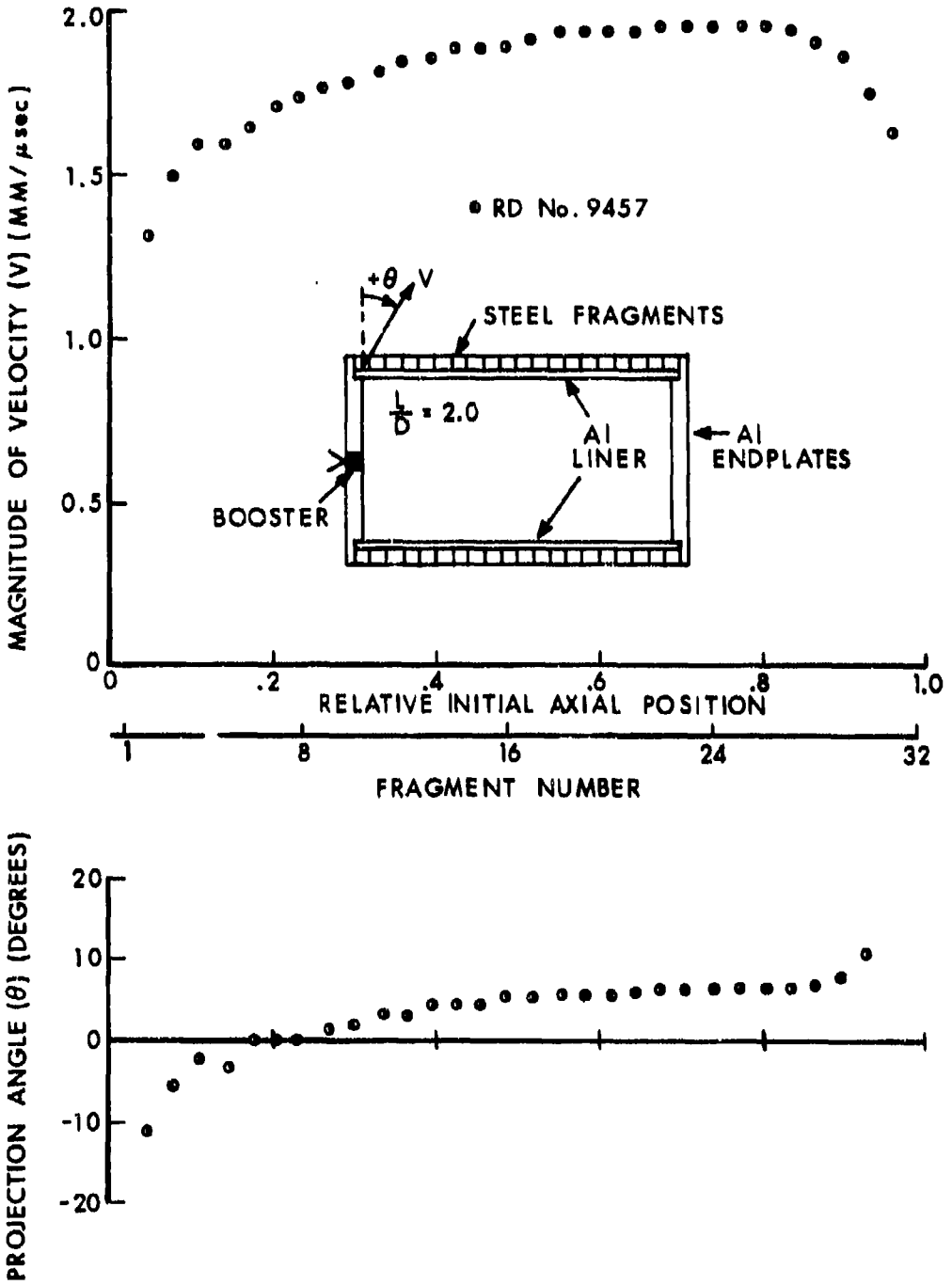

Figure 13. Preformed-Fragment Warhead with Al Liner and Al Endplates, L/D = 2.0: Fragment Speed and Projection Angle Distribution

If the standard form of the HEMP code is used to predict the performance of discrete-fragment warheads without including the effects of fragment separation and subsequent explosive gas leakage between fragments, the dashed line results shown in Figure 14 are obtained. Shown in Figure 14 is a comparison between these HEMP calculations and experimental data of fragment speed and projection angle distributions for an L/D = 1.0 cylindrical warhead. In the HEMP calculations the fragments are modeled as a fluid, i.e., the fragments cannot accommodate a tensile force but they can be recompressed. This would be a logical approach with a continuum code since the fragments are not a continuum but discrete particles which will separate with the application of a small tensile force. It is obvious that this modeling is superior in predictive ability than the prediction of velocity and angle by Gurney and Taylor, also shown in Figure 14. However, the agreement between the HEMP computations and experiment is not as good as desired. Because of this and other objections[5], modeling of the effects of fragment separation and explosive gas leakage between fragments was initiated to improve the overall predictive capability of the computations.

The discrete-fragment warhead (missile warhead) model presented involves the following three essential features: A) modeling of the discrete-fragments, B) modeling of fragment separation and subsequent explosive gas leakage and, C) criteria for fragment separation and method to determine this criteria.

A. Modeling of Discrete-Fragments

When discrete-fragments are placed on a cylindrical body, whether it be the bare explosive or a liner containing the explosive, (assuming conventional fragment shapes) air gaps will occur between the fragments in the circumferential direction. Consequently, the discrete-fragment casing forms a composite of metal and air. In reality, this is a three-dimensional system. However, the approach that was adopted with the two-dimensional modeling is similar to the methods used in the modeling of composite materials. The discrete metal-air composite casing (metal preformed-fragments) is modeled as a homogeneous continuous material of the same metal material as the experimental fragments, but with the requirement that the total mass of the new continuous metal casing equal the total mass of all the fragments on the experimental warhead. For example, in the case of cubical fragments, the resulting continuous metal casing wall thickness in the model will be less than one of the sides of

---

[5] *Karpp, R. R. and Predebon, W. W., "Calculations of Fragment Velocities from Fragmentation Munitions," First International Symposium on Ballistics, Orlando, Florida, 13-15 November 1974, Section IV, pp. 145-176, Proceedings Published by American Defense Preparedness Association, Union Trust Building, Washington, DC.*

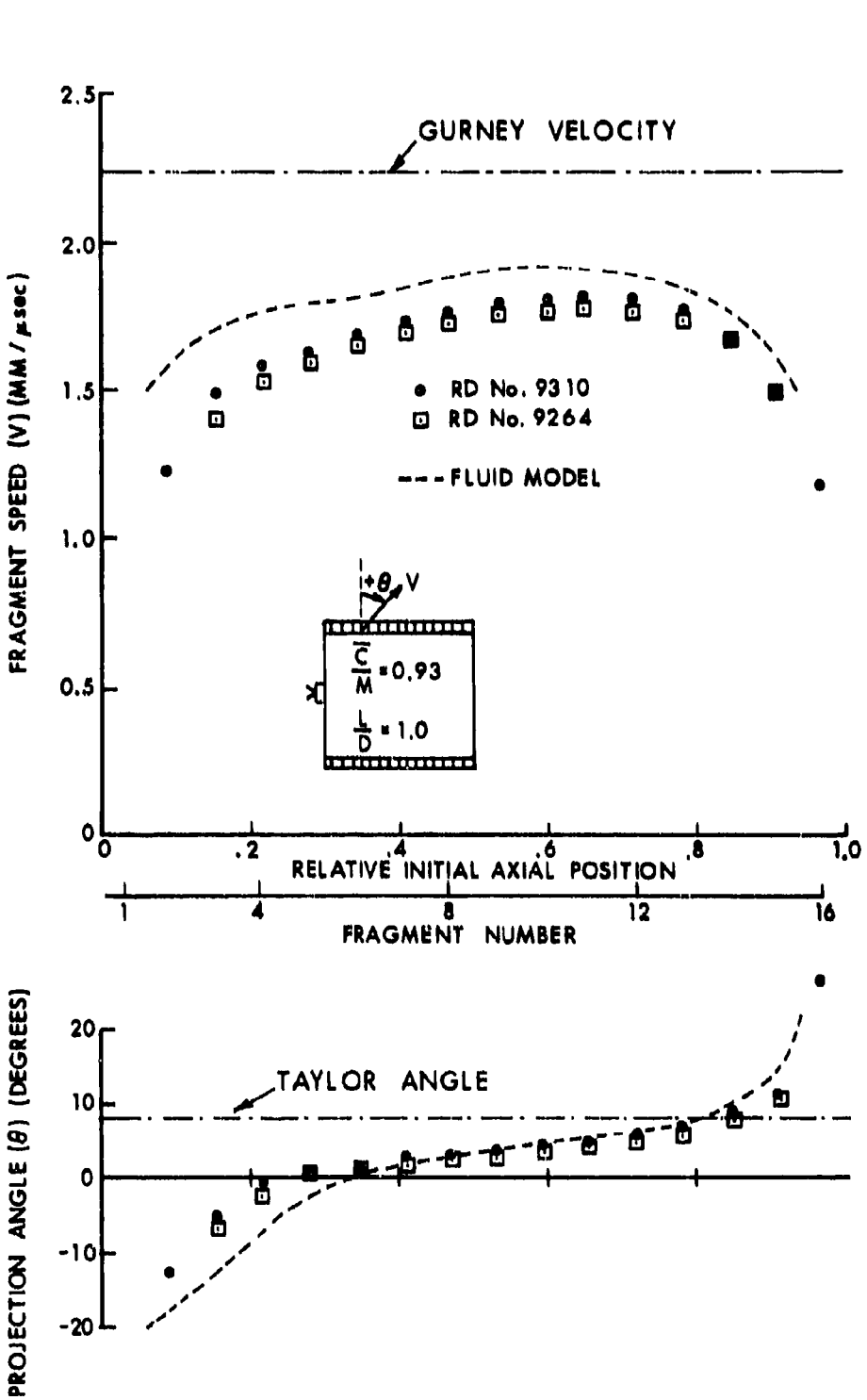

Figure 14. Comparison of Gurney Velocity and Taylor Angle with HEMP (Fluid Model) Computations and Experimental Data, L/D = 1.0 Cylindrical Preformed-Fragment Warhead

an actual cubical fragment. For a cylindrical warhead, the modeled casing outside diameter for a given explosive diameter is obtained from

$$M_T = \sum_i m_i = \rho_f \left\{ \frac{\pi}{4} l_W \left(D_M^2 - D_{HE}^2 \right) \right\} ,$$

where M_T is the measured total fragment mass (plus liner mass if the warhead has a liner), m_i are the measured individual fragment masses, ρ_f is the fragment density, l_W is the total length of the fragments on the warhead, D_{HE} is the measured diameter of the explosive and D_M is the outside diameter of the continuous metal casing to be computed. If one ignores the air gap between the fragments and uses the fragment cube dimension as the continuous casing wall thickness, then for the cases reported in Sections II and IV, the modeled total mass will be as much as 6% greater than the actual total mass.

B. Fragment Separation and Explosive Gas Leakage

The general ideas of the model for fragment separation and explosive gas leakage will be presented here; however, the specific details and equations have been presented in an earlier report[5].

The HEMP code models continuum behavior in general. However, in reality, when fragment separation occurs a continuous casing circumference ceases to increase. But the standard form of the code causes the casing to remain continuous. This treatment tends to yield a higher radial acceleration and thus a higher final fragment velocity. This can be corrected by computing the true force acting on an element of the casing. The true force is computed in the code by reducing the pressure acting on the interface of the casing by the factor R_b/R, where R_b is the radius at fragment separation and R is the current radius. At present, R_b must be determined by experiment. After fragment separation, i.e., $R > R_b$, a void appears between fragments and gas leakage occurs. This effect is modeled in the code by calculating the rate of efflux from an ideal nozzle passing its maximum rate of flow. The rate of efflux is computed in the code for every cycle, and the mass leaked for a single cycle is the product of the mass rate and the cycle time increment. In this manner, the model accounts for gas leakage between fragments after casing breakup. Gas leakage reduces the pressure accordingly. Lastly, to simulate a loss in circumferential stress upon casing breakup, the yield strength of the fragment material is set equal to zero when $R > R_b$.

C. Criterion for Fragment Separation

Currently, the criterion for fragment separation, R_b, is an empirically determined quantity. As discussed in Section II the fragments

are all premarked and recovered in a soft recovery medium (Celotex) after firing. The recovered fragments are weighed and measured for their dimensions. Obtained from these measurements is the fragment plastic deformation due to the explosive loading (or final dimensions). Since its original dimensions are known a straight forward calculation determines the corresponding radius of the warhead at which the fragments separated. (The elastic displacements are neglected in this analysis). For the case of cubical fragments on bare explosive for L/D = 1.0 and 2.0 cases, the expansion ratio at fragment separation, i.e., R_b/R_o where R_o is the inside radius of the casing, was found to be 1.2. The recovered fragment measurements and expansion ratios are tabulated in Table I. This criterion for fragment separation is empirical; the criterion will not be applicable in general. Thus, the next refinement in this analysis is to relate this criterion to a fundamental material property.

IV. COMPARISON BETWEEN COMPUTATIONAL AND EXPERIMENTAL RESULTS

In Figures 15-17 are shown comparisons between the calculations with the discrete-fragment model (labeled Elastic-Plastic with Gas Leakage Model) and experimental results. In Figure 15 and 16 the calculated fragment speed and projection angle distributions are compared with the experimental data for L/D = 1.0 and 2.0 cylindrical warheads, respectively. Data from two test firings are plotted in each figure. In both cases the agreement between computation and experiment is extremely good. Also shown in Figures 15 and 16 are the calculations without the discrete-fragment model, namely, a fluid model, and the Gurney velocity and Taylor angle predictions. Shown in Figure 17 is a comparison between the computations and experimental data for the same case as shown in Figure 16 except with dual-end axial initiation. Again the agreement between computation and experiment is very good. Note that the computations model the region where the two detonation waves collide (higher pressure region) at 0.5 relative initial axial position.

Returning to the test results shown in Figure 13, note that the warhead configuration in Figure 13 is similar to the configuration in Figure 16. Both are L/D = 2.0 cylindrical warheads with the same explosive material, fragment material and size, and with essentially the same explosive diameter. However, the test warhead in Figure 13 has a liner between the explosive and fragments, and endplates. The reasons given for placing the liner between the fragments and the explosive are often varied. It was the intent of this initial experiment, in conjunction with computational modeling (yet to be performed), to help explain the effect of a liner on warhead performance. Due to the additional width of the Al liner, the inside fragment radius increased, which resulted in more fragments on the warhead, and thus a larger total metal weight, and lower C/M. These data are given in Table 1 by Rd. No. 9457. Consequently, the results of Figures 13 and 16 cannot be directly compared. However, it is the authors' judgment at this time, based on these data and other

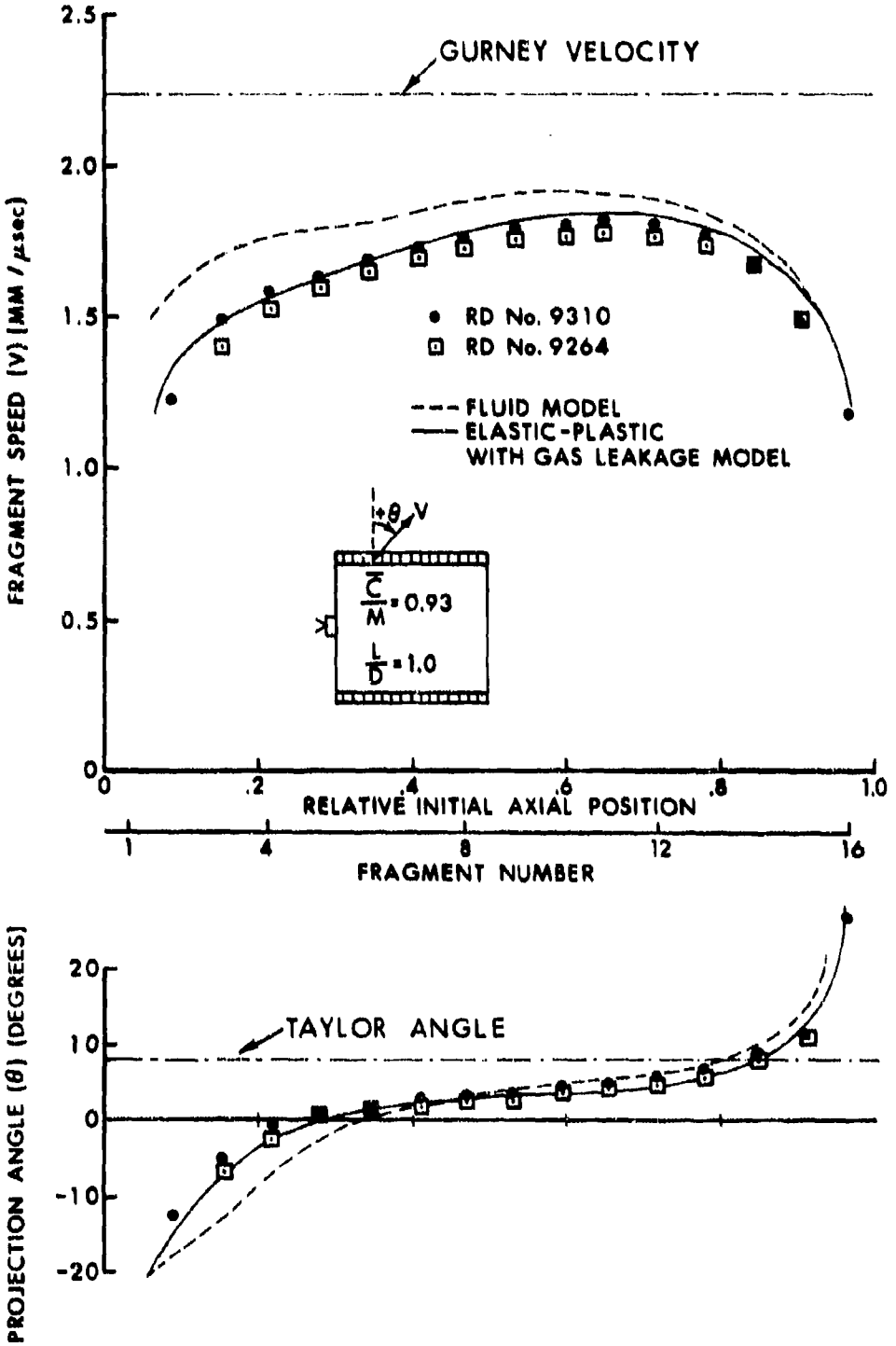

Figure 15. Comparison of Fluid Model Computations and Discrete-Fragment Model Computations with Experimental Data, L/D = 1.0 Cylindrical Preformed-Fragment Warhead

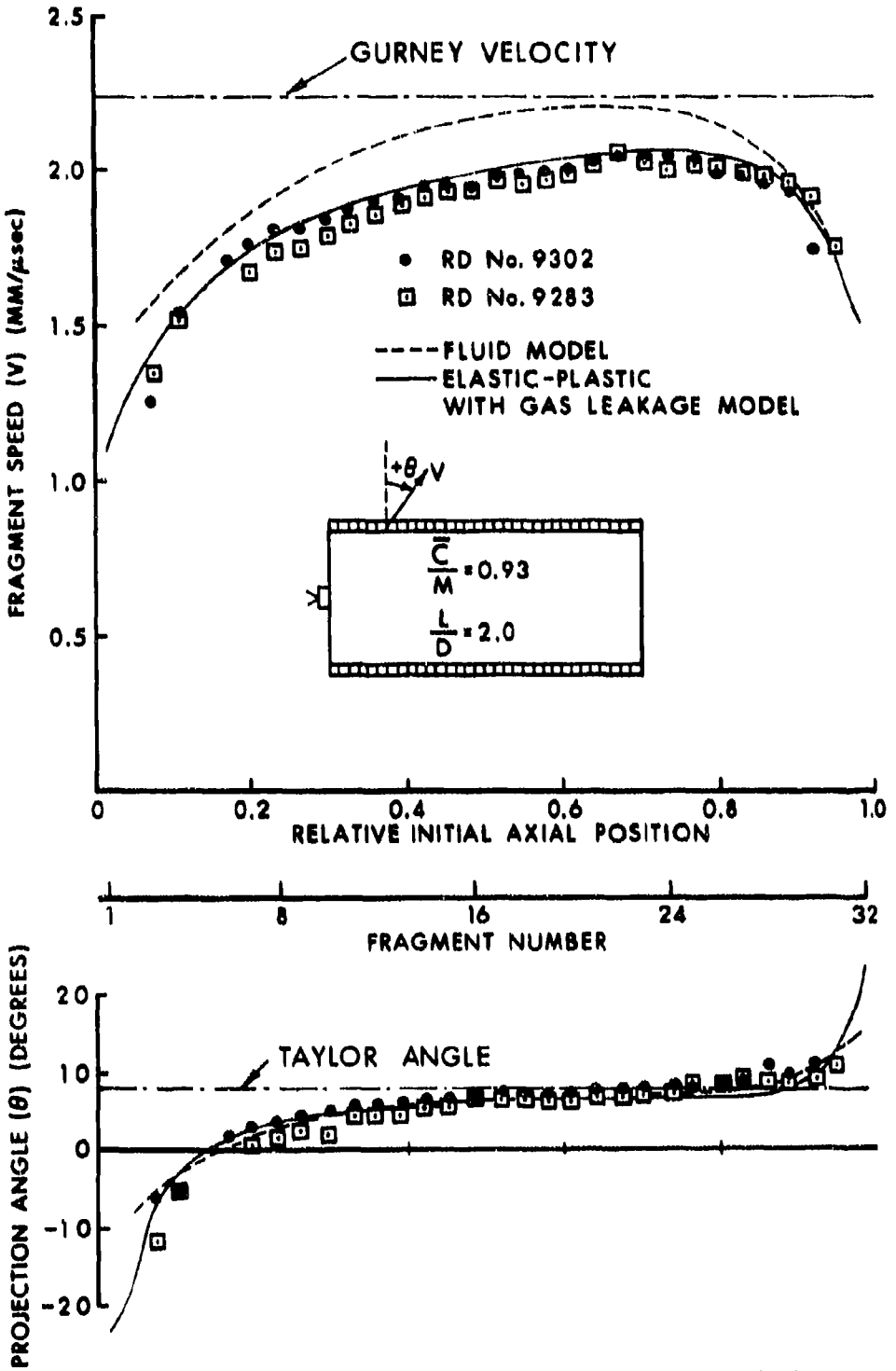

Figure 16. Comparison of Fluid Model Computations and Discrete-Fragment Model Computations with Experimental Data, L/D = 2.0 Cylindrical Preformed-Fragment Warhead

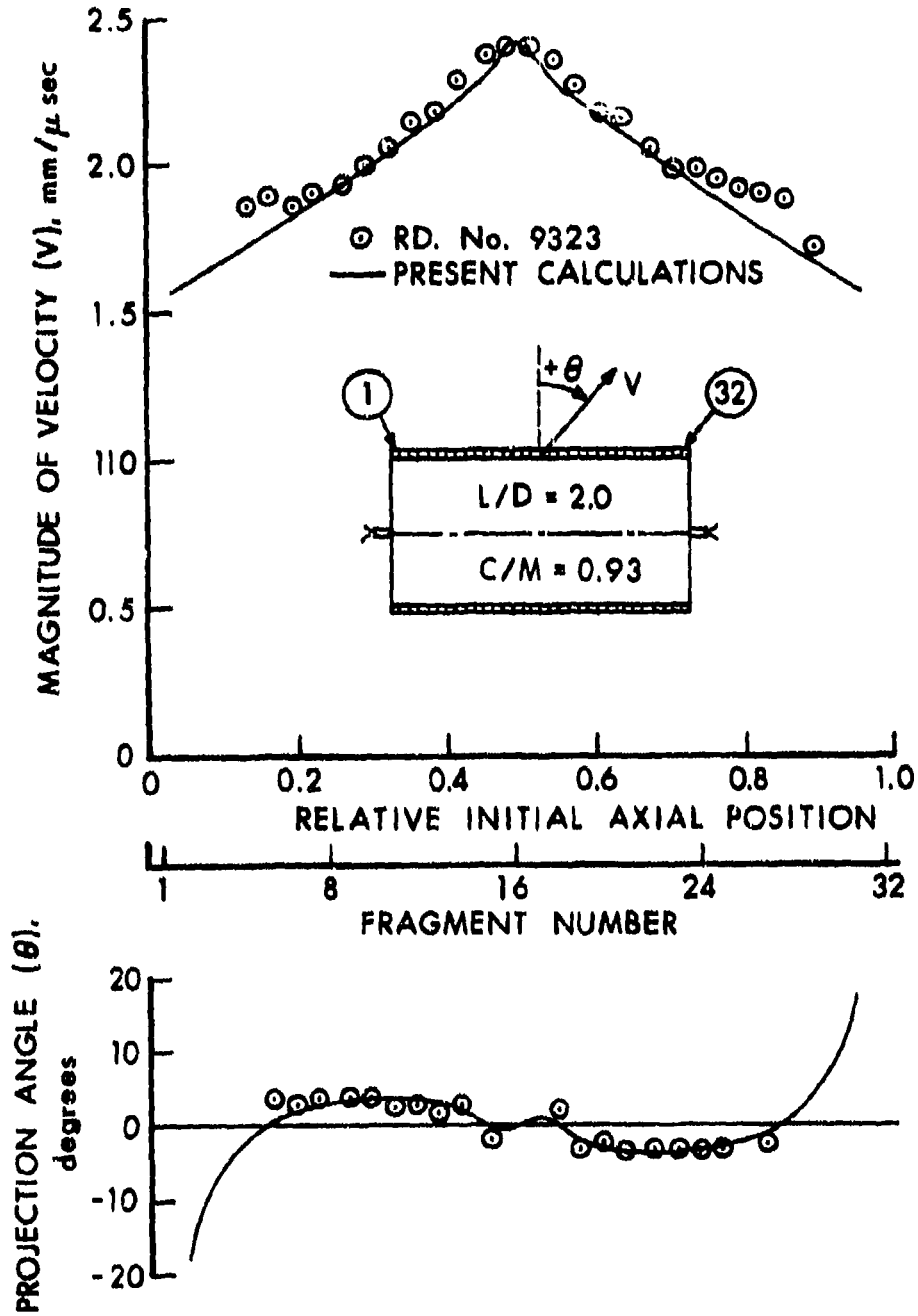

Figure 17. Comparison of Discrete-Fragment Model Computations with Experimental Data for L/D = 2.0 Cylindrical Preformed-Fragment Warhead with Dual End Axial Initiation

calculations, that the effect of a liner is to contain the explosive gases for a longer period of time. This in turn causes leakage of explosive gases between fragments to occur at a larger expansion ratio, resulting in a higher final fragment speed, as compared to the case without a liner (assuming all other quantities being equal). This can be illustrated from a plot[6] of calculated fragment speed versus time (from detonation) for these cases. From a plot of this type one observes that fragment separation and leakage occurs during the initial, approximately exponential, acceleration rise. By placing a liner between the fragments and explosive, one can prolong fragment separation and subsequent leakage until the fragment speed versus time profile flattens, which then results in a higher final fragment velocity. From these and other computations, it is estimated that up to approximately a 10% increase in final fragment velocity can be obtained with a liner between the fragments and explosive versus the case without a liner.

Having demonstrated extremely good agreement between the present calculations and experimental data for both L/D = 1.0 and 2.0 cylindrical warheads with single-end and dual-end axial initiation, the computations were then confidently utilized, without experimental verification, to study the effect of initiation posture on warhead performance. Shown in Figure 18 are the nine initiation postures that were computed. The cylindrical warheads that are drawn in Figure 18 are all with a length (L) to diameter (D) ratio of two and initiated as shown. The first case of dual end axial booster initiation, i.e., initiation with two 19.05 mm diameter explosive boosters, is shown in Figure 17. The computational results of the remaining eight cases are shown respectively in Figures 19-26. Shown in Figure 17 and Figures 19-26 is the effect of a large variety of initiation postures on warhead performance. The general idea of this set of computations is, on the one hand, to demonstrate the versatility and generality of this computational tool, and on the other hand to aid in the understanding of the effect of initiation posture on warhead performance. Furthermore, should the initiation posture of interest lie somewhere between these cases, a simple interpolation of the already computed cases is all that is required for a first approximation of the warhead performance. Similarly, since the computational results are general, i.e., scalable, then if the geometry of interest is not precisely the same as the cases calculated, these results can be scaled up or down assuming proper scaling procedures are followed. Lastly, it is worth while to note that axial line initiation, Figure 26, is the one case of the initiation variations studied in which the fragment projection angle and speed distribution are significantly different from the dual end axial initiation case, Figure 17.

Shown in Figures 27 through 30 are the computational results for two different internal cavity sizes and materials for the same general L/D = 2.0 cylindrical geometry. Shown in Figure 27 are the results for

---

[6] *Karpp, R. R. and Predebon, W. W., "Calculations of Fragment Velocities from Fragmentation Munitions," p. IV-164.*

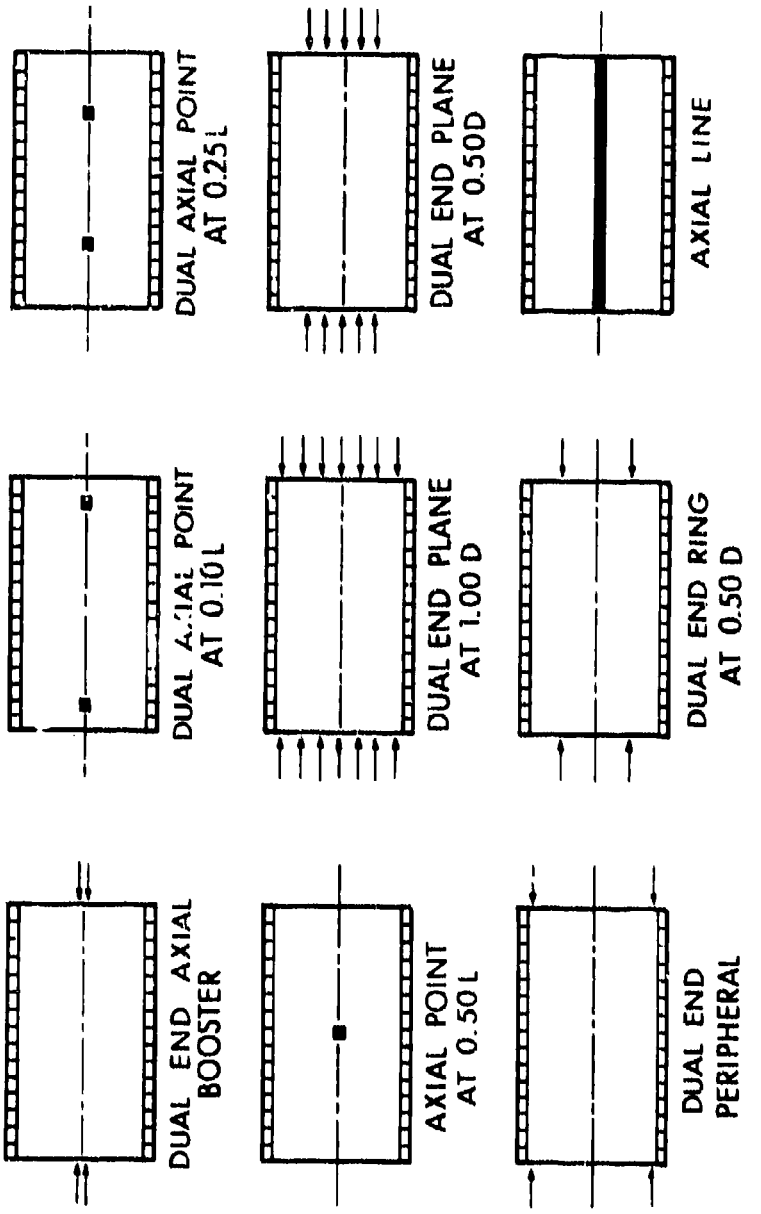

Figure 18. Initiation Postures

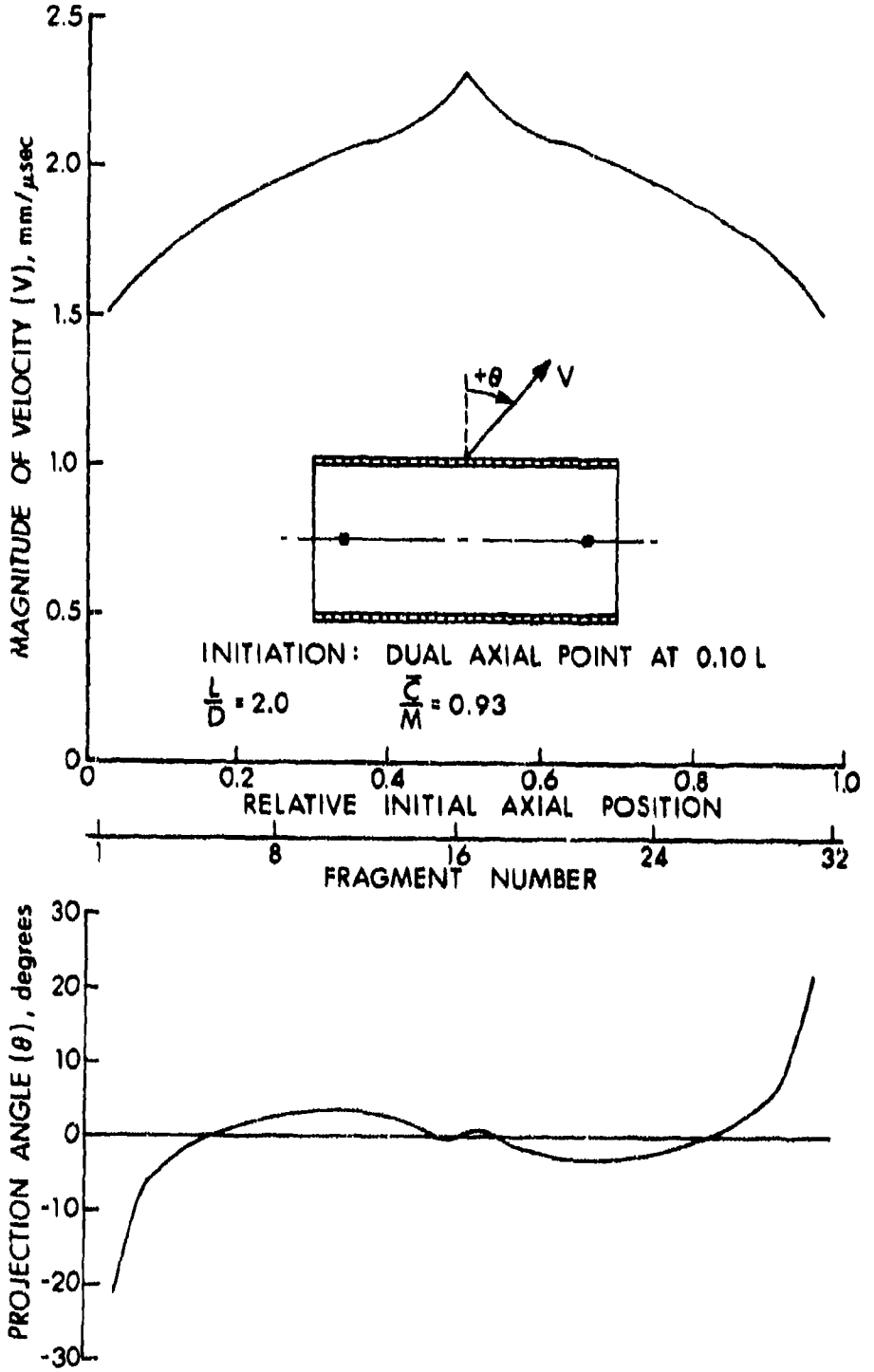

Figure 19. Calculations of Fragment Speed and Projection Angle Distributions for L/D = 2.0 Cylindrical Preformed-Fragment Warheads with Dual Axial Point Initiation at 0.10 L

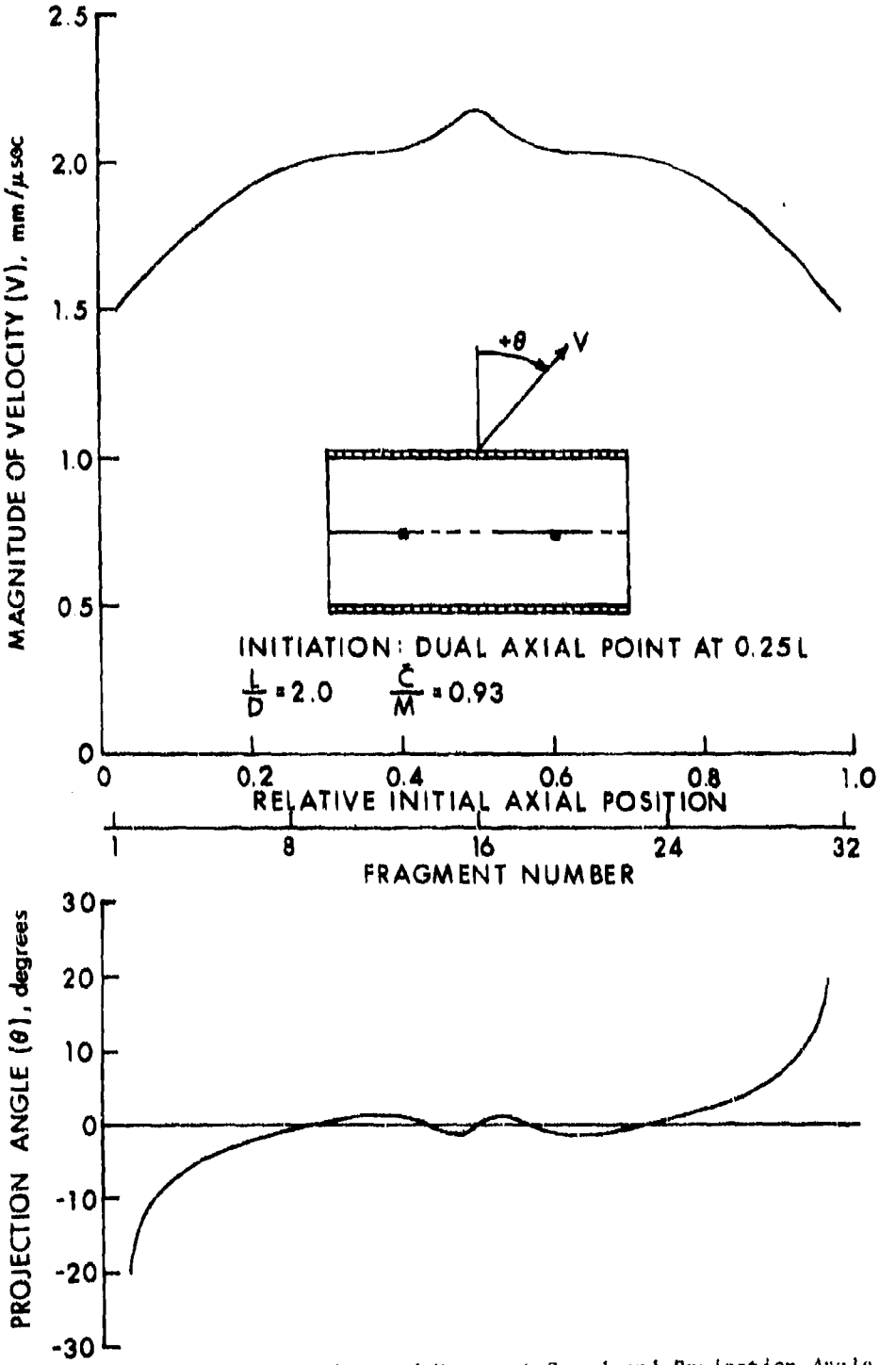

Figure 20. Calculations of Fragment Speed and Projection Angle Distributions for L/D = 2.0 Cylindrical Preformed-Fragment Warheads with Dual Axial Point Initiation at 0.25 L

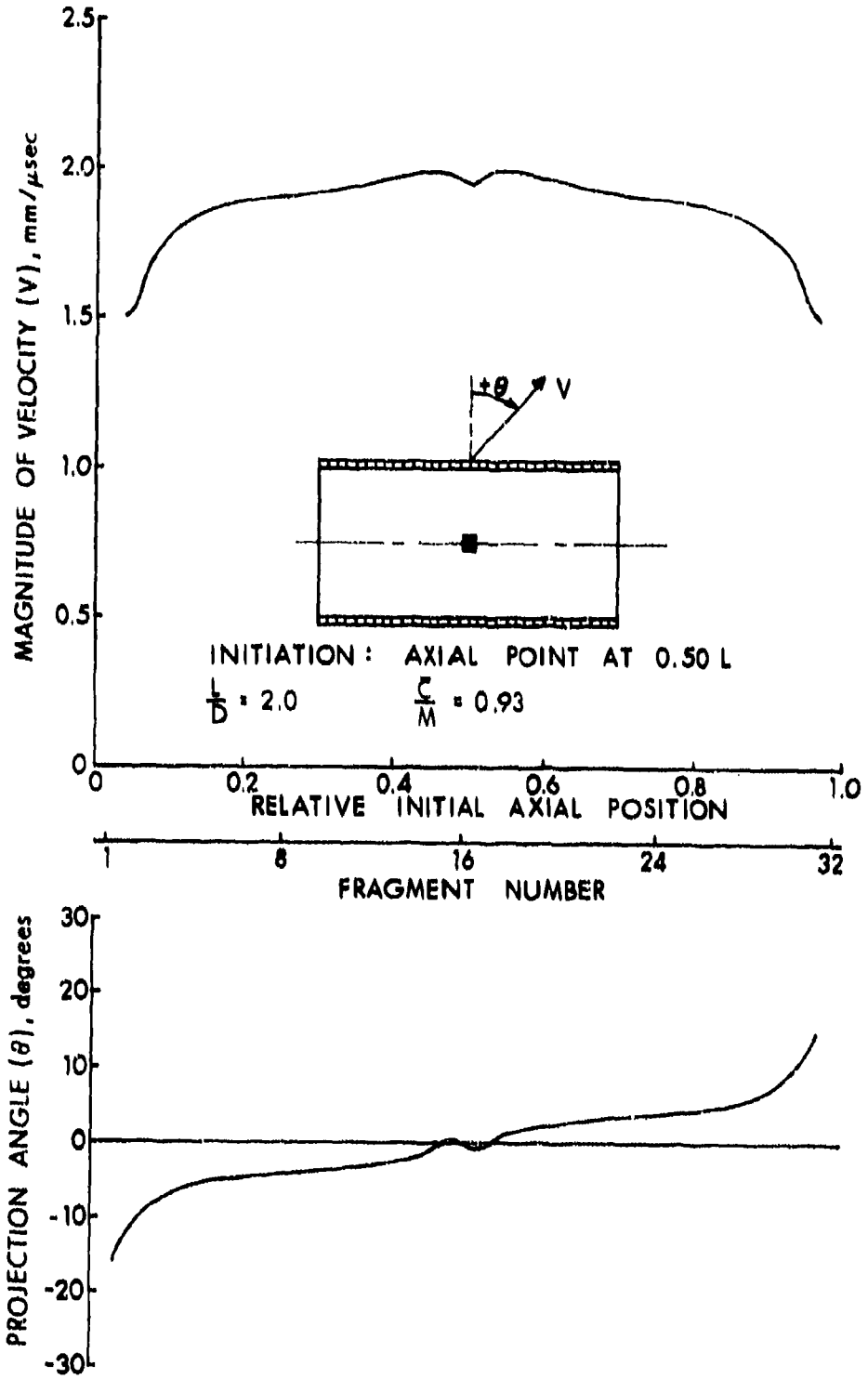

Figure 21. Calculations of Fragment Speed and Projection Angle Distributions for L/D = 2.0 Cylindrical Preformed-Fragment Warheads with Axial Point Initiation at 0.50 L

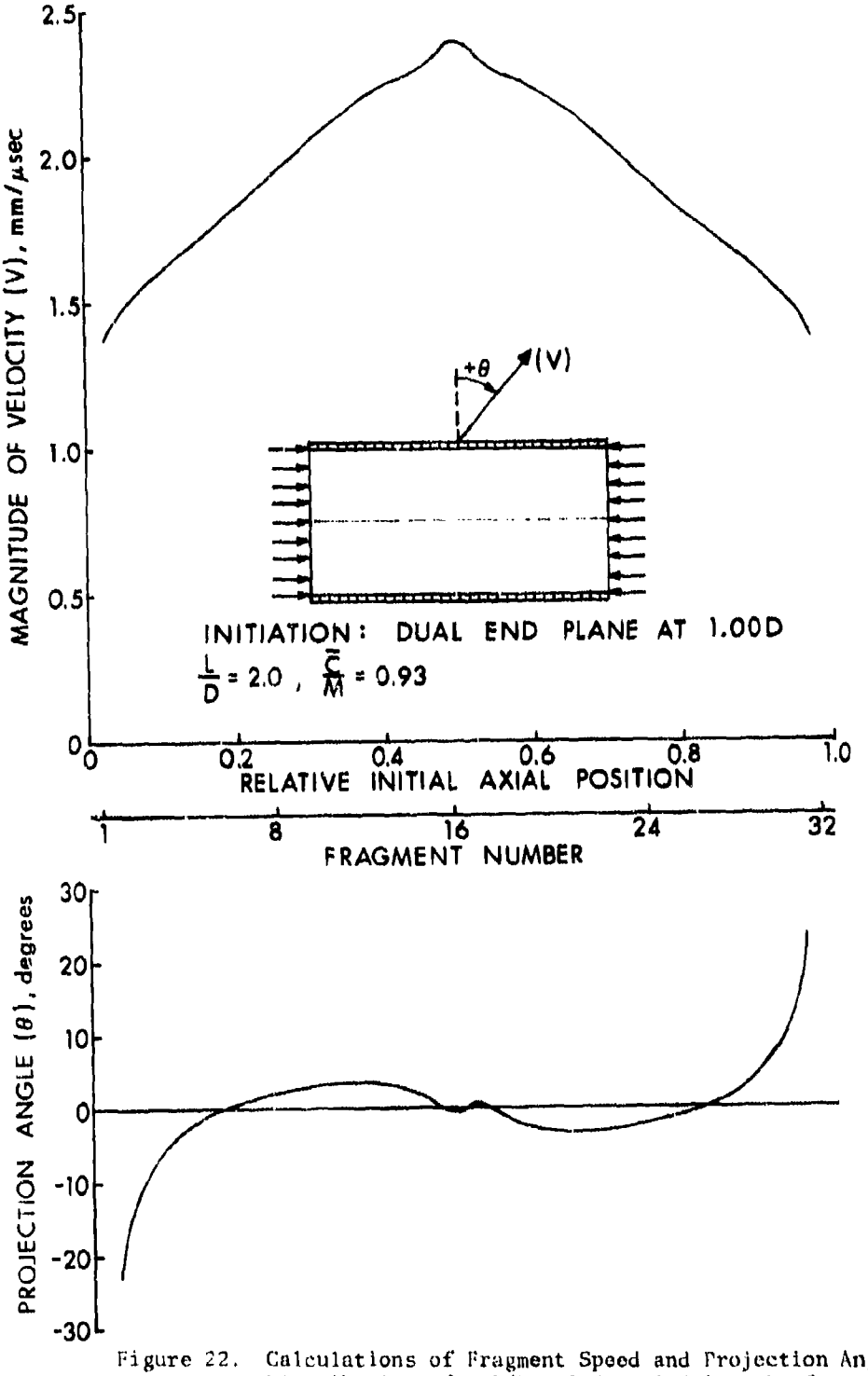

Figure 22. Calculations of Fragment Speed and Projection Angle Distributions for L/D = 2.0 Cylindrical Preformed-Fragment Warheads with Dual End Plane Initiation at 1.00 D

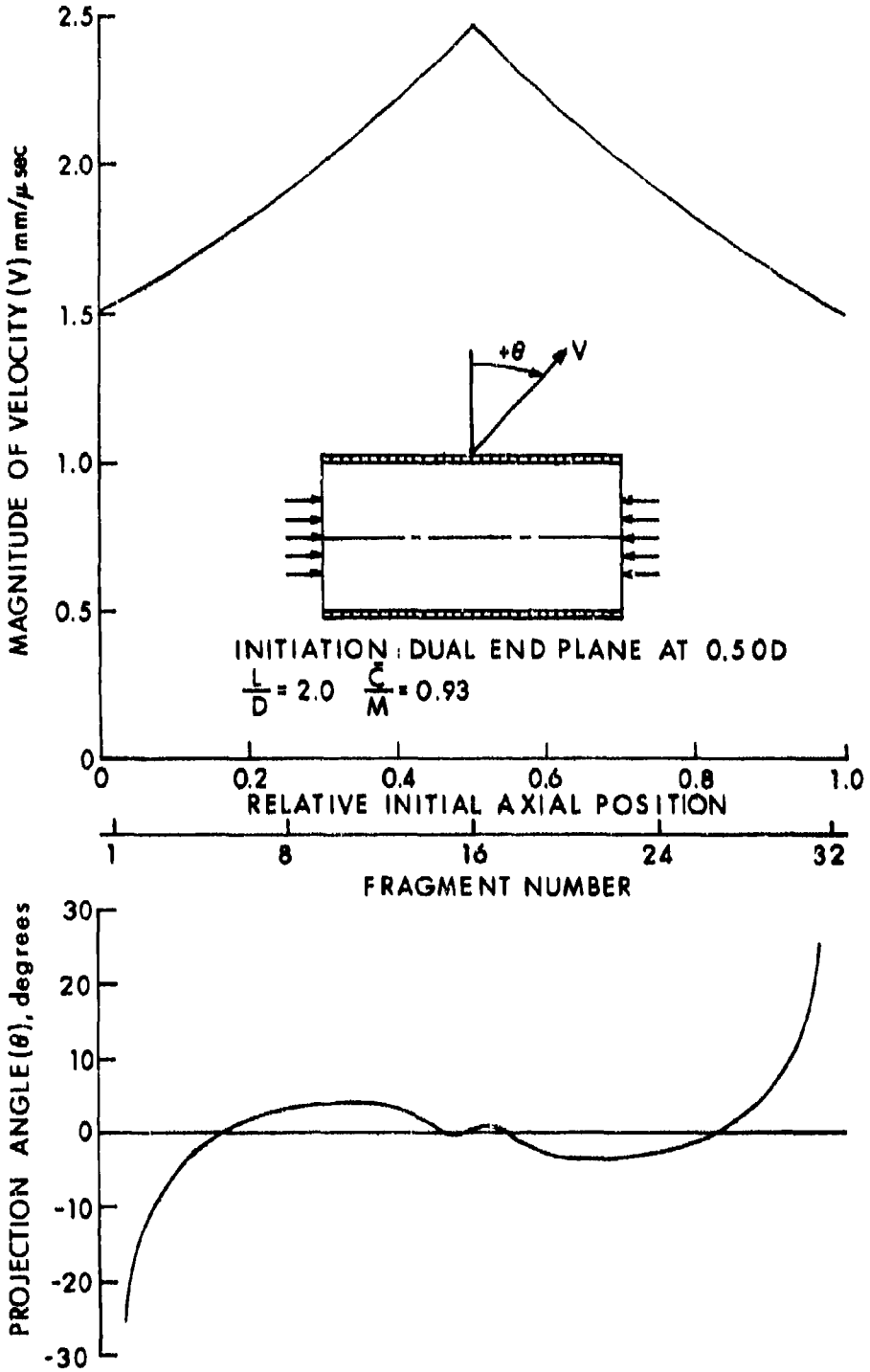

Figure 23. Calculations of Fragment Speed and Projection Angle Distributions for L/D = 2.0 Cylindrical Preformed-Fragment Warheads with Dual End Plane Initiation at 0.50 D

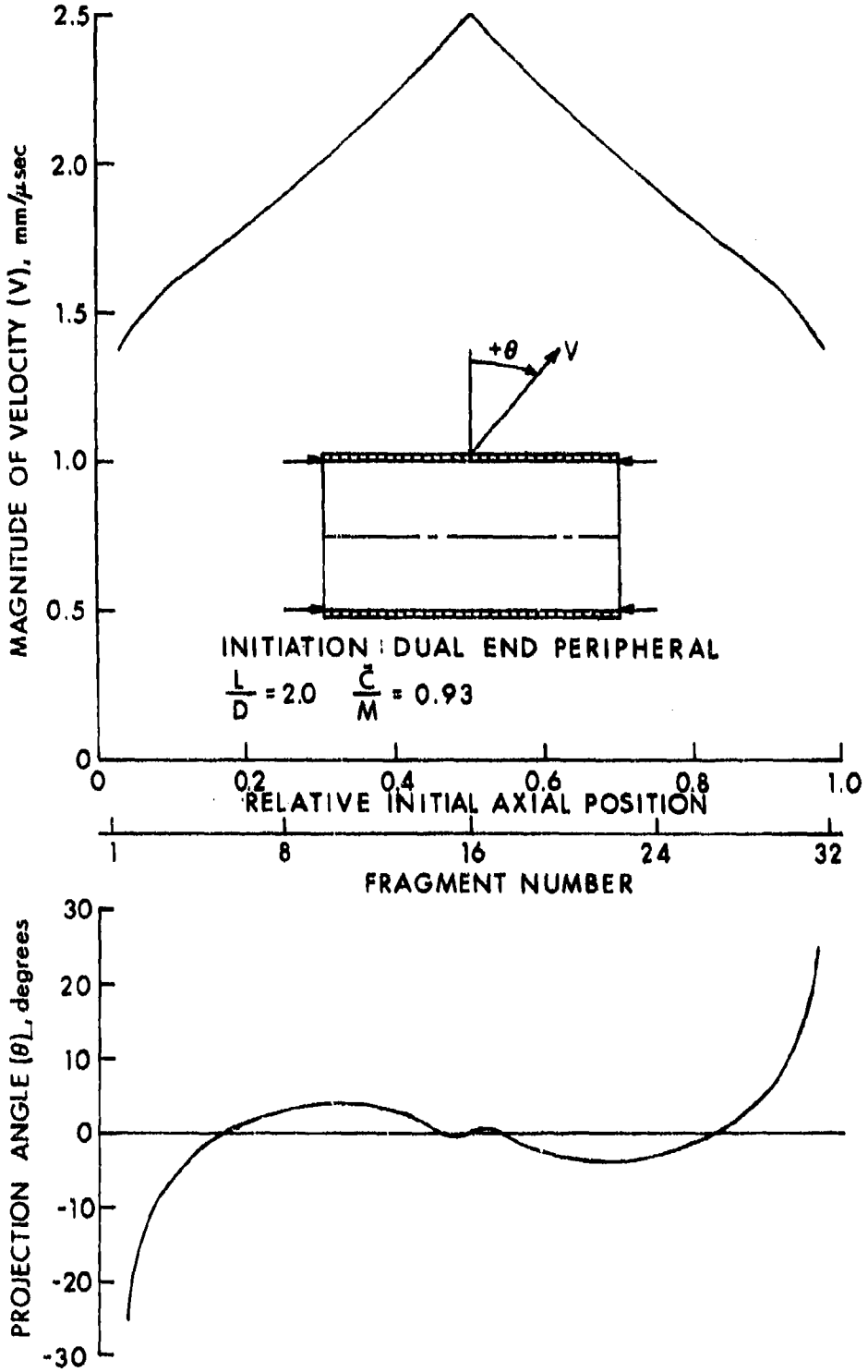

Figure 24. Calculations of Fragment Speed and Projection Angle Distributions for L/D = 2.0 Cylindrical Preformed-Fragment Warheads with Dual End Peripheral Initiation

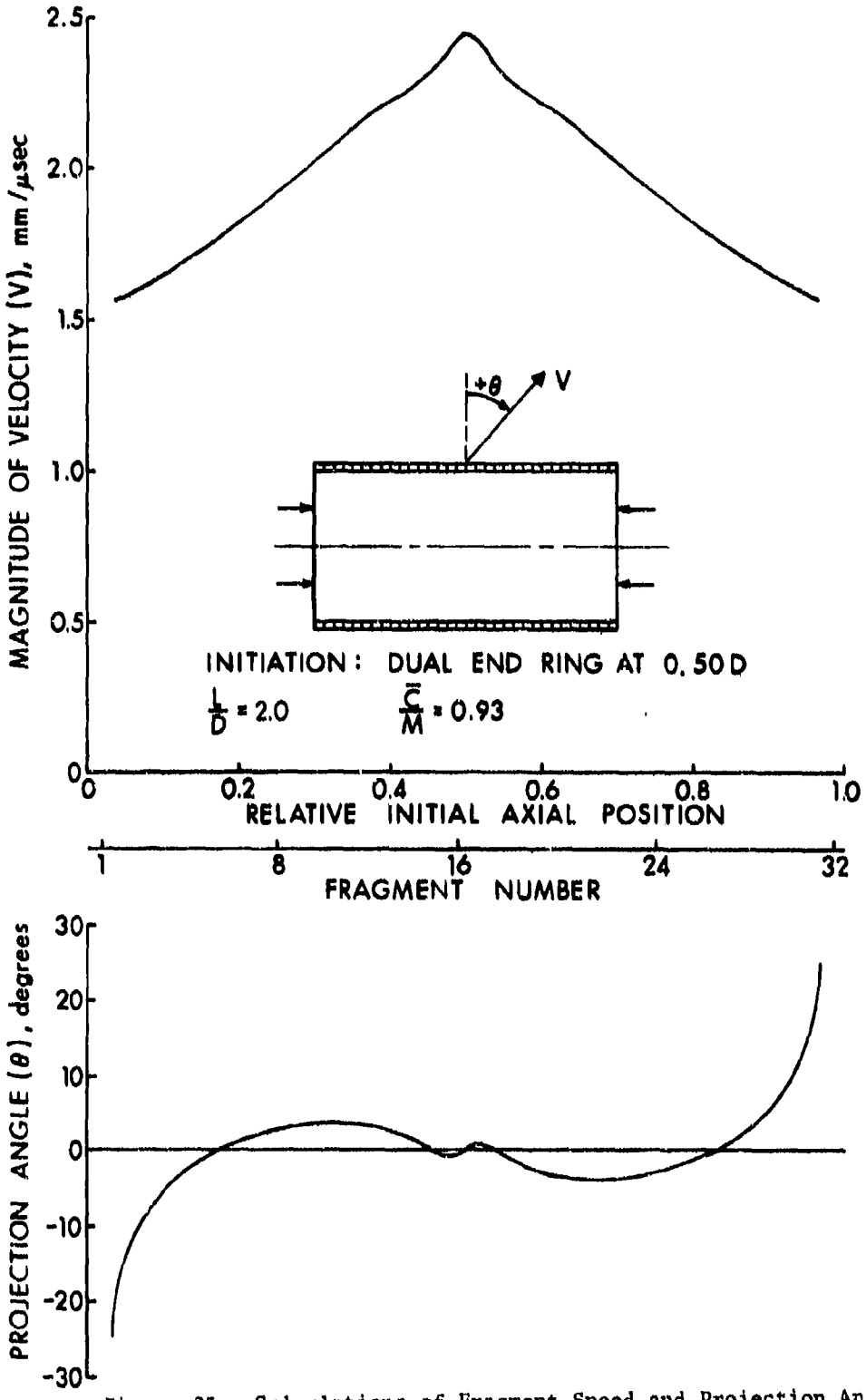

Figure 25. Calculations of Fragment Speed and Projection Angle Distributions for L/D = 2.0 Cylindrical Preformed-Fragment Warheads with Dual End Ring Initiation at 0.50 D

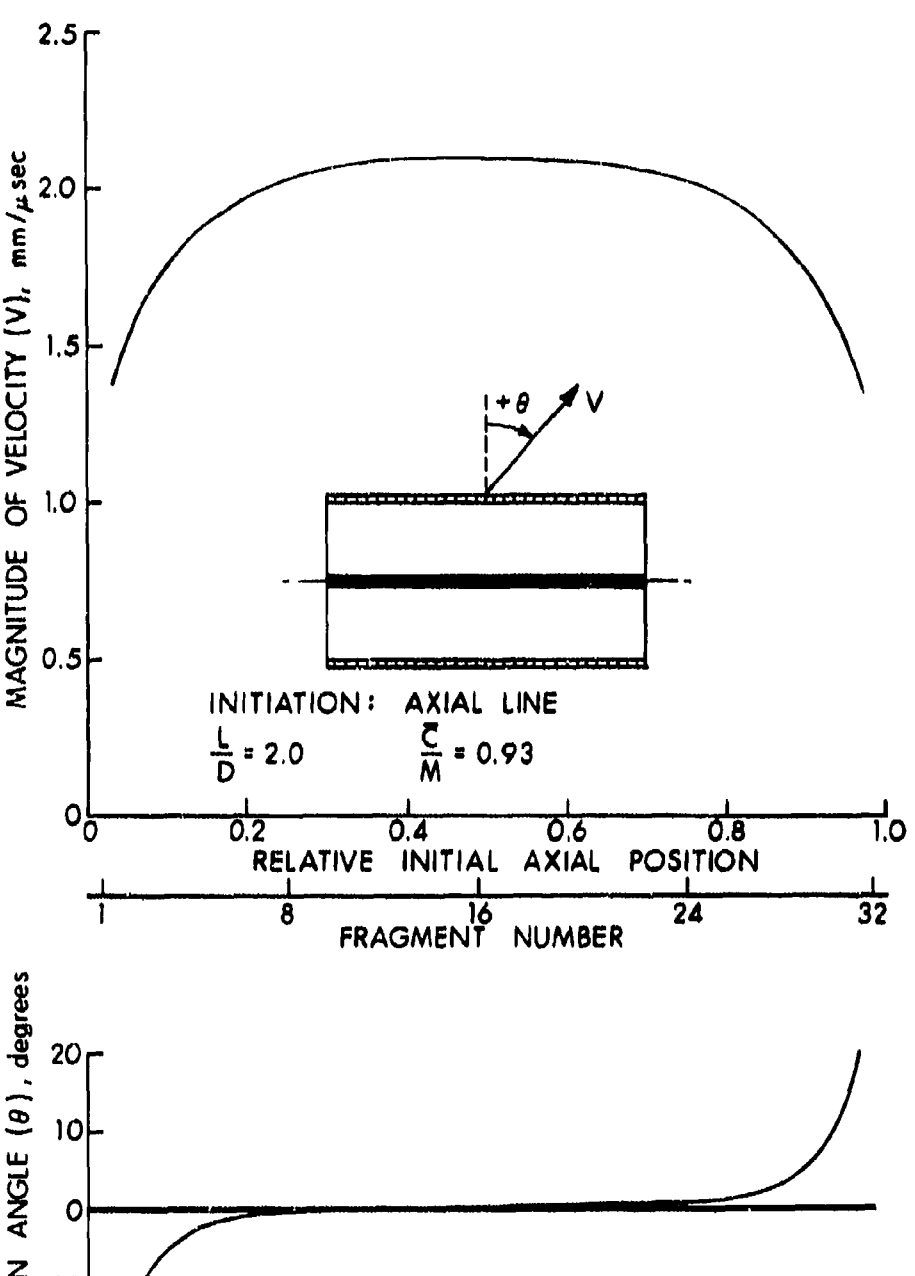

Figure 26. Calculations of Fragment Speed and Projection Angle Distributions for L/D = 2.0 Cylindrical Preformed-Fragment Warheads with Axial Line Initiation

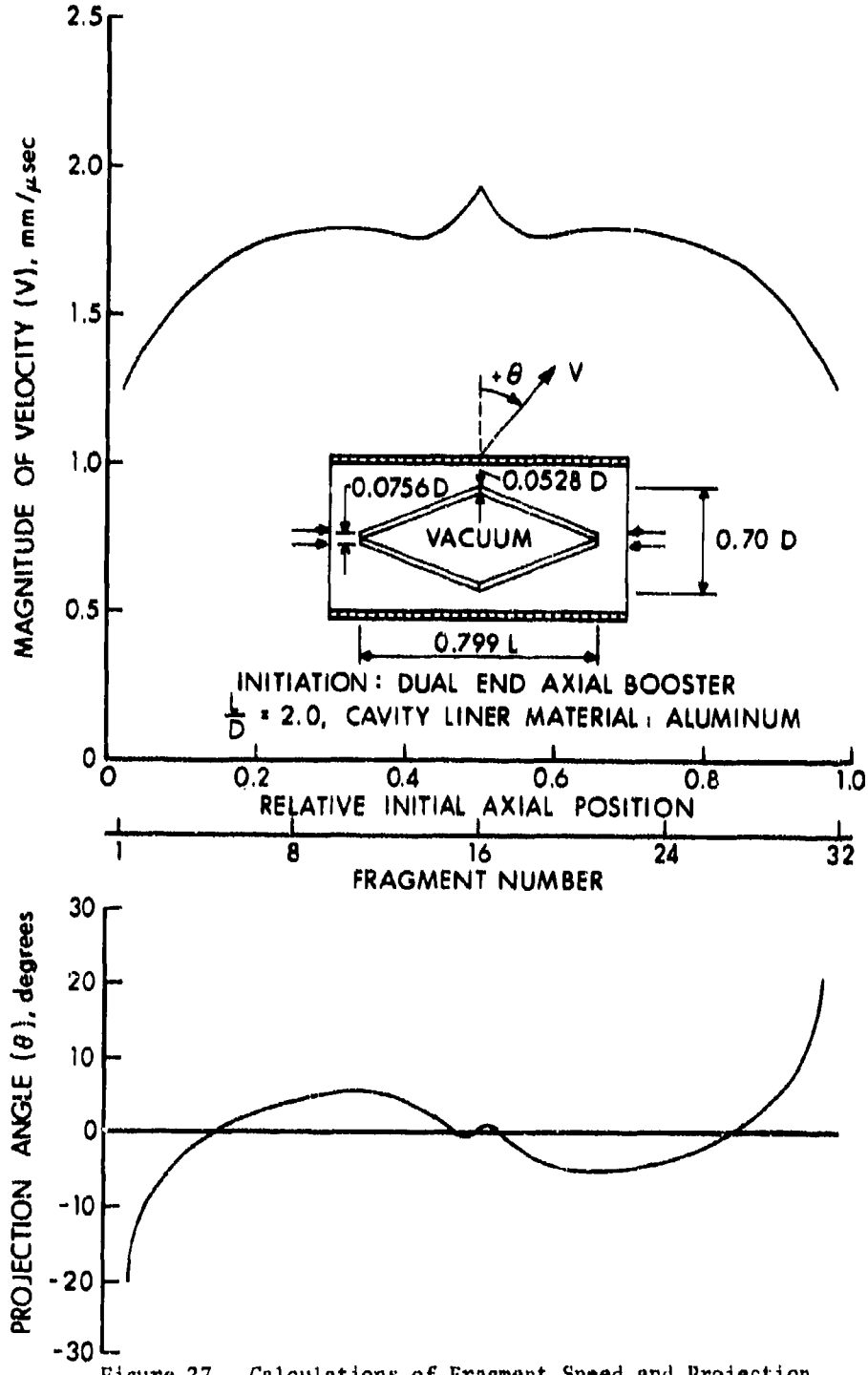

Figure 27. Calculations of Fragment Speed and Projection Angle Distributions for an L/D = 2.0 Cylindrical Preformed-Fragment Warhead with Internal Aluminum Cavity Liner and Dual End Axial Initiation

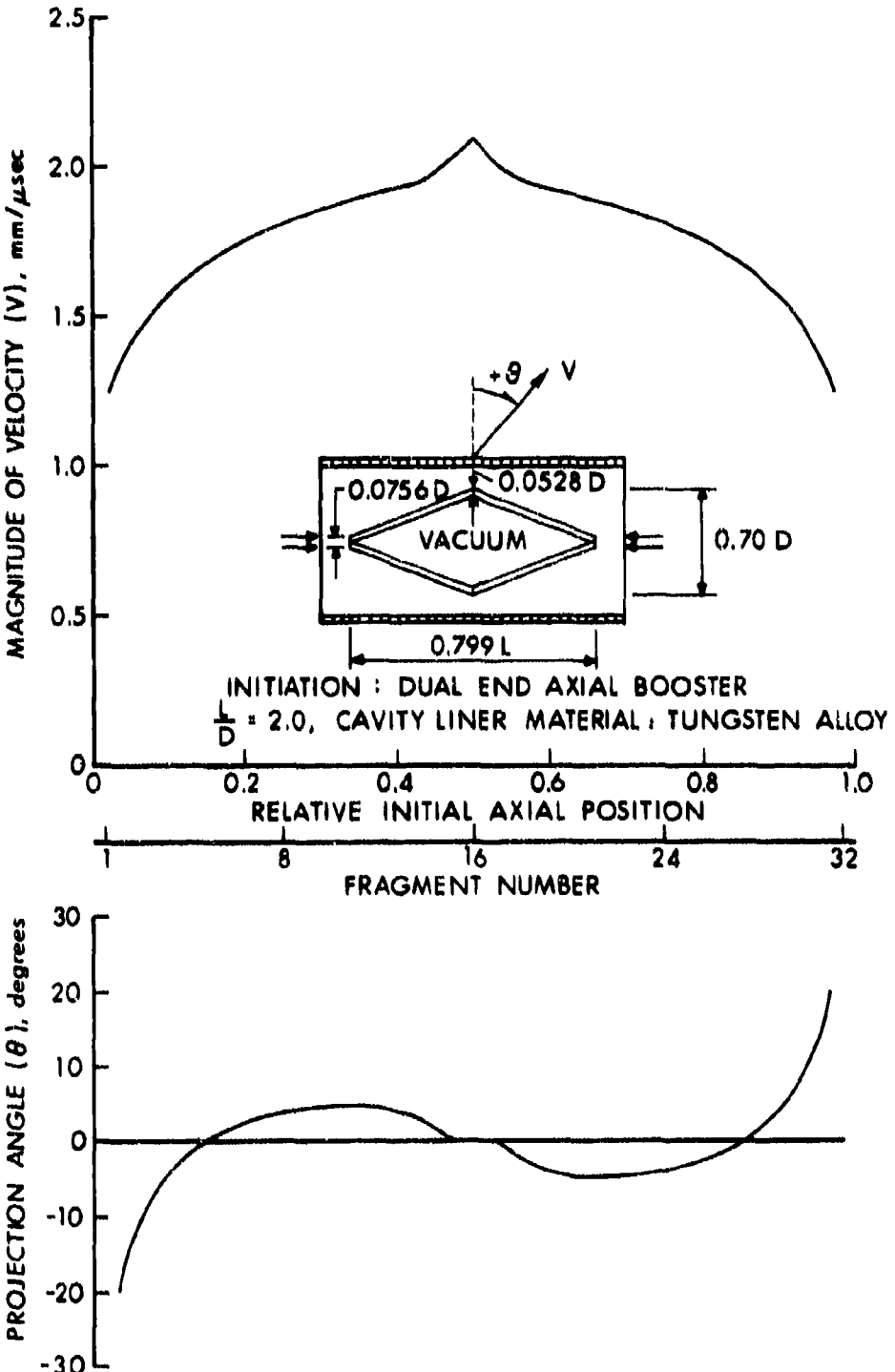

Figure 28. Calculations of Fragment Speed and Projection Angle Distributions for an L/D = 2.0 Cylindrical Preformed-Fragment Warhead with Internal Tungsten Alloy Cavity Liner and Dual End Axial Initiation

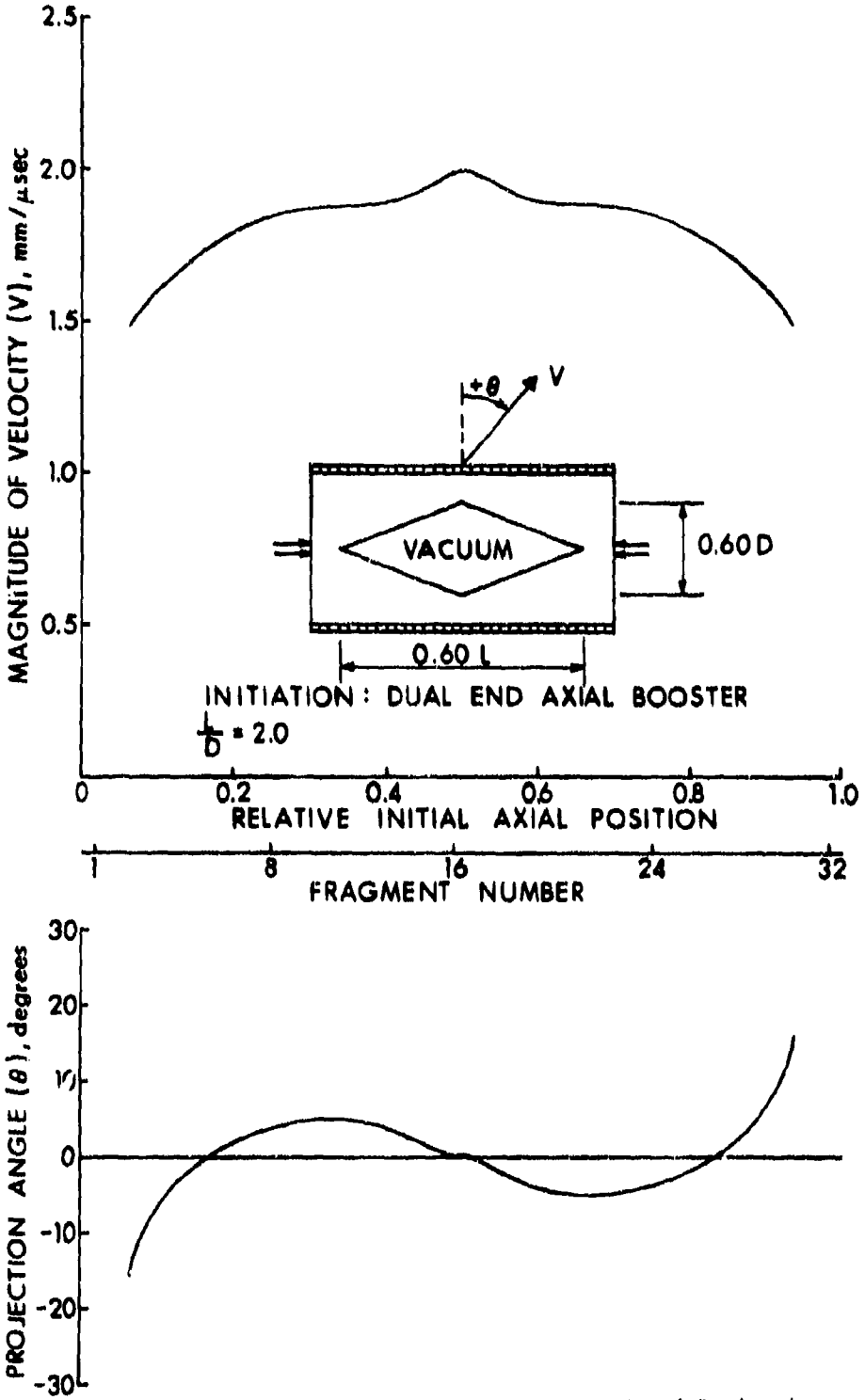

Figure 29. Calculations of Fragment Speed and Projection Angle Distributions for an L/D = 2.0 Cylindrical Preformed-Fragment Warhead with an Internal Cavity Modeled as a Vacuum and Dual End Axial Initiation

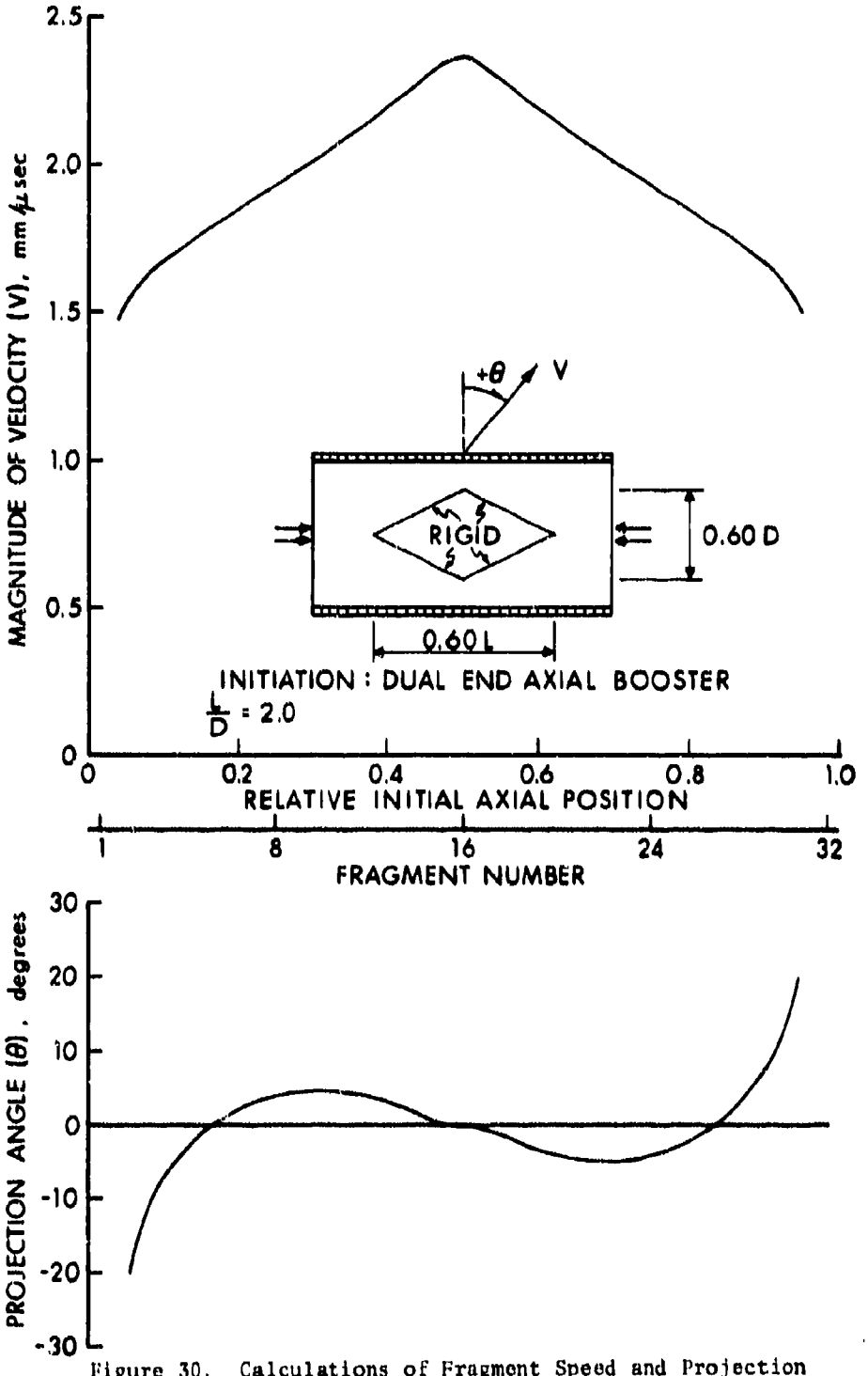

Figure 30. Calculations of Fragment Speed and Projection Angle Distributions for an L/D = 2.0 Cylindrical Preformed-Fragment Warhead with an Internal Cavity Modeled as Rigid and Dual End Axial Initiation

the case with an aluminum cavity liner material with the dimensions as indicated. Comparing the results shown in Figure 27 with those in Figure 17 it can be seen that although the projection angle distribution is only slightly altered, the fragment speed is significantly reduced.

The computational results with a tungsten alloy (ρ = 16890 KG/M^3) cavity liner material for the same cylindrical geometry and cavity shape given in Figure 27 are shown in Figure 28. As expected, due to the higher density cavity liner material the fragment speed distribution is somewhat higher than with aluminum; however, the fragment projection angle distribution is not noticeably altered. It is important to note that these results are for one cavity shape and therefore are not necessarily true for all cavity shapes and sizes. In Figures 29 and 30 are shown the computational results for a slightly different cavity size where the cavity is modeled either as a vacuum (Figure 29) or as a cavity whose boundaries are rigid (Figure 30) for all time. The purpose of these two computations is to provide a qualitative lower (Figure 29) and upper (Figure 30) bound on fragment speed and projection angle distributions that can be expected for the cylindrical geometry and cavity shape shown.

V. CONCLUSIONS AND RECOMMENDATIONS

A discrete-fragment warhead (missile warhead) computational modeling capability has been developed which is capable of modeling with a satisfactory degree of confidence the performance of a large variety of axisymmetric warhead configurations. The computational warhead model includes the ability to model the effects of varying L/D, fragment material and size, explosive material, initiation posture, and internal cavity material and shape. It is felt that the modeling capability can be extended to include two layers of fragments on the warhead, a liner between the fragments and the explosive, and end confinement. The experiments were completed for these cases and are discussed in Section II.

Future efforts should include additional experiments and computational modeling with different liner materials, shapes and sizes, and end confinement to understand fully the influence of these variables on warhead performance. Also, future work should include generalization of the empirical criterion for fragment separation to a more fundamental criterion. For example, material properties, such as the total plastic strain to failure, might be used to predict fragment separation.

It is also believed that the modeling capability can successfully be applied to certain aspects of eccentric warheads (a three dimensional problem). However, while some degree of success may be had, in order to model eccentric warheads properly, a three dimensional computer code is needed.

ACKNOWLEDGEMENTS

The authors wish to thank Dr. Robert R. Karpp for the many helpful technical discussions during the course of the work. Also the authors are grateful to Mr. G. Gentle and Mr. Carroll West for their assistance with the experimental program.

LIST OF SYMBOLS

$\bar{C}/M$	Nominal charge (explosive) mass to metal mass (fragment + liner) ratio
D_{HE}	Explosive diameter
D_M	Calculated outside diameter of continuous metal casing model, from $M_T = \rho_f \{\pi/4\ L_W\ (D_M^2 - D_{HE}^2)\}$
L_c	Side of a cubical fragment
L_{HE}	Explosive Length
L_W	Length of fragments on warhead (equal to L_{HE} in all cases)
M_c	Mass of a cubical fragment (also equivalent to m_i)
M_{HE}	Mass of the explosive charge
M_R	Mass of a rod
m_i	Individual fragment mass
M_{RC}	Mass of a recovered cubical fragment
M_T	Total mass of fragments and liner on warhead
N_{cc}	Number of cubical fragments per column (along warhead length)
N_c	Number of columns of cubical fragments
N_R	Number of rods per warhead
R	Current warhead radius in computations
R_b	Radius of warhead at fragment separation in computations
R_{b/R_o}	Expansion ratio at fragment separation or breakage ratio; equivalent to W_{RC}/L_c
R_o	Initial inside radius of casing (metal fragments)
W_{RC}	Recovered cube dimension in the circumferential (hoop) direction.
α_f	Azimuthal fragment-bearing sector angle
ρ_f	Fragment mass density

DISTRIBUTION LIST

No. of Copies	Organization
12	Commander Defense Documentation Center ATTN: DDC-TCA Cameron Station Alexandria, VA 22314
1	Director Defense Advanced Research Projects Agency ATTN: Tech Info 1400 Wilson Boulevard Arlington, VA 22209
1	Commander US Army Materiel Development and Readiness Command ATTN: DRCDMA-ST 5001 Eisenhower Avenue Alexandria, VA 22333
1	Commander US Army Materiel Development and Readiness Command ATTN: DRCDL 5001 Eisenhower Avenue Alexandria, VA 22333
1	Commander US Army Aviation Research and Development Command ATTN: DRSAV-E 12th and Spruce Streets St. Louis, MO 63166
1	Director US Army Air Mobility Research and Development Laboratory Ames Research Center Moffett Field, CA 94035
2	Commander US Army Electronics Command ATTN: DRSEL-RD DRSEL-HL-CT, S.Crossman Fort Monmouth, NJ 07703
3	Commander US Army Missile Research and Development Command ATTN: DRDMI-R DRDMI-RFS DRDMI-RDP, H.W. Burnam Redstone Arsenal, AL 35809
1	Commander US Army Tank Automotive Research & Development Command ATTN: DRDTA-RWL Warren, MI 48090
2	Commander US Army Mobility Equipment Research & Development Command ATTN: Tech Docu Cen, Bldg. 315 DRSME-RZT Fort Belvoir, VA 22060
1	Commander US Army Armament Materiel Readiness Command Rock Island, IL 61202
1	Commander US Army Armament Research and Development Command ATTN: DRSAR-CG Dover, NJ 07801
5	Commander US Army Armament Research and Development Command ATTN: DRDAR-LC, Dr. J. Frasier DRDAR-LCA, Dr. E. G. Sharkoff Mr. L. Rosendorf Mr. G. Randers-Pehrson Mr. J. Pearson Dover, NJ 07801

DISTRIBUTION LIST

No. of Copies	Organization
5	Commander US Army Armament Research and Development Command ATTN: DRDAR-LCE, Dr. R.Walker DRDAR-TS-S DRDAR-LC, Mr. R. Nixon Dover, NJ 07801
1	Commander US Army Harry Diamond Labs ATTN: DRXDO-TI 2800 Powder Mill Road Adelphi, MD 20783
2	Commander US Army Materials and Mechanics Research Center ATTN: J. Mescall D. Roylance Watertown, MA 02172
1	Commander US Army Natick Research and Development Command ATTN: DRXRE, Dr. D. Sieling Natick, MA 01762
1	Director US Army TRADOC Systems Analysis Activity ATTN: ATAA-SL (Tech Lib) White Sands Missile Range NM 88002
1	Deputy Assistant Secretary of the Army (R&D) Department of the Army Washington, DC 20310
1	HQDA (DAMA-CSM) Washington, DC 20310
1	HQDA (DAMA-ARP) Washington, DC 20310
1	HQDA (DAMA-MS) Washington, DC 20310
1	Commander US Army Research Office ATTN: Dr. E. Saibel P. O. Box 12211 Research Triangle Park NC 27709
1	Commander US Naval Air Systems Command ATTN: AIR-604 Washington, DC 20360
1	Commander US Naval Ordnance Systems Cmd ATTN: ORD-9132 Washington, DC 20360
1	Chief of Naval Research ATTN: Code ONR 439, N.Perrone Washington, DC 20360
1	Commander US Naval Air Development Ctr Johnsville Warminster, PA 18974
1	Commander US Naval Missile Center Point Mugu, CA 93041
2	Commander David W. Taylor Naval Ship Research & Development Center ATTN: D. R. Garrison A. Wilner Bethesda, MD 20034
3	Commander US Naval Surface Weapons Center ATTN: Code TEB, D.W.Colbertson Mr. L. Hock Code TX, Dr. W.G. Soper Dahlgren, VA 22448

DISTRIBUTION LIST

No. of Copies	Organization
2	Commander US Naval Surface Weapons Center ATTN: WR-13 Tech Library Silver Spring, MD 20910
6	Commander US Naval Weapons Center ATTN: J. Pearson, Code 383 J.S. Rinehart, Code 383 M. Backman, Code 3831 C.F. Austin, Code 3833 R.G.S. Sewell, Code 3835 J. Weeks, Code 3266 China Lake, CA 93555
2	Commander US Naval Research Laboratory ATTN: Tech Lib J. Baker Washington, DC 20375
1	Superintendent US Naval Postgraduate School ATTN: Dir of Lib Monterey, CA 93940
1	AFATL (Mr. Leonard T. Wilson) Eglin AFB, FL 32542
3	AFATL (DLRD, K. McArdle; DLRV, G. Crews; DLYD) Eglin AFB, FL 32542
1	ADTC/DLJW (CPT D. Matuska) Eglin AFB, FL 32542
1	AFATL (DLDL, MAJ J.E. Morgan) Eglin AFB, FL 32542
2	AFWL (WLL) Kirtland AFB, NM 87117
1	ASD (ASBRS) Wright-Patterson AFB, OH 45433
2	AFML Wright-Patterson AFB, OH 45433
1	AFFDL (FDT) Wright-Patterson AFB, OH 45433
3	ASD (YH/EX, John Rievley; XRHD, Gerald Bennett; ENYS, Matt Kolleck) Wright-Patterson AFB, OH 45433
1	Headquarters National Aeronautics and Space Administration Washington, DC 20546
2	Director National Aeronautics and Space Administration John F. Kennedy Space Center ATTN: KN-ES-3 KN-ES-34 Kennedy Space Center, FL 32899
2	Director National Aeronautics and Space Administration Langley Research Center ATTN: R. J. Hayduk Tech Lib Hampton, VA 23665
1	US Energy Research and Development Administration Los Alamos Scientific Lab ATTN: Mr. R. Craig, MS-960 Dr. L. Hantel, WX-2 Dr. Robert Karpp Los Alamos, NM 87544